Compression experiments to 126 GPa and 2500 K and thermal equation of state of Fe3S: Implications for sulphur in the Earth's core

Compression experiments to 126 GPa and 2500 K and thermal equation of state of Fe_3S: Implications for sulphur in the Earth's core

Samuel Thompson[1], Tetsuya Komabayashi[1], Helene Breton[1], Sho Suehiro[2], Konstantin Glazyrin[3], Anna Pakhomova[3], and Yasuo Ohishi[4]

[1]School of GeoSciences and Centre for Science at Extreme Conditions, University of Edinburgh EH9 3FE, UK

[2]Department of Earth and Planetary Sciences, Tokyo Institute of Technology, Tokyo 152-8551, Japan

[3]Deutsches Elektronen-Synchrotron (DESY), Photon Science, Notkestrasse 85, 22607 Hamburg, Germany

[4]SPring-8, Japan Synchrotron Radiation Research Institute, 1-1-1 Kouto, Sayo-cho, Sayo-gun, Hyogo 679-5198, Japan

*corresponding author: Samuel Thompson

E-mail: s1335012@sms.ed.ac.uk

Abstract

Pressure-volume-temperature (*P*-*V*-*T*) experiments on Fe_3S were conducted to 126 GPa and 2500 K in laser-heated diamond anvil cells (DAC) with in-situ X-ray diffraction (XRD). Seventy nine high-*T* data as well as four 300-K data were collected, based on which new thermal equations of state (EoS) for Fe_3S were established. The room-*T* data together with existing data were fitted to the third order Birch-Murnaghan EoS, which yielded, K_0 = 126 ± 2 GPa and K' = 5.1 ± 1 with V_0 fixed at 377.0 $Å^3$. A constant αK_T term in the thermal pressure equation, Pth = $\alpha K_T(T\text{-}300K)$, fitted the high-*T* data well to the highest temperature, which implies that the contributions from the anharmonic and electronic terms should be minor in the thermal pressure term. The high-*T* data were also fitted to the Mie-Grüneisen-Debye model; γ_0 = 1.01 ± 0.03 with θ_0 and q fixed at 417 K and 1 respectively. Calculations from the EoS show that crystalline Fe_3S at 4000-5500 K is denser than the Earth's outer core and less dense than the inner core. Assuming a density reduction due to melting, liquid Fe_3S would meet the outer core density profile, which however suggests that no less than 16 wt%S is needed to reconcile the observed outer core density deficit. The S-rich B2 phase, which was suggested to be a potential liquidus phase of an Fe_3S-outer core above 250 GPa, namely the main constituent of its solid inner core, would likely be less dense than the Earth's inner core. As such, while the outer core density requires as much sulphur as 16 wt%, the resulting liquidus phase cannot meet the density of the inner core. Any sulphur-rich composition should therefore be rejected for the Earth's core.

Key words: Earth's core, Fe-S alloys, equation of state, high-pressure, diamond anvil cell, in-situ XRD

1. Introduction

Seismological observations of the Earth's interior indicate that the Earth's core is composed of a solid inner core and liquid outer core. The major component of the cores is believed to be iron while a 4-7 % density deficit is observed compared to pure iron at the relevant pressure (*P*) and temperature (*T*) conditions (Birch, 1952; Komabayashi, 2014). This density deficit has been associated with the presence of light elements in the core (Poirier, 1994). Over 60 years since the first proposition by Birch (1952), the light element in the core is yet to be defined. Estimates of core composition have been made through study of iron meteorites (Goldstein et al., 2009; Williams et al., 2006), which are thought to be representative of the cores of small terrestrial bodies. Geochemical estimates were also made through study of mantle-derived samples and chondritic meteorites (McDonough and Sun, 1995; Palme and O'Neill, 2003), which provided information on the relative depletion of elements in the mantle versus solar abundances. In all lines of study, a small number of candidate elements have been identified: Si, S, O, C, and H (Hirose et al., 2013; Poirier, 1994). Of these candidate elements, sulphur has been most extensively studied (Hirose et al., 2013); the system Fe-S is currently of significant interest (Campbell et al., 2007; Ozawa et al., 2013; Mori et al., 2017; Tateno et al., 2019a). Nevertheless, recent core formation models included silicon and oxygen as the major light elements in the core as a consequence of metal-silicate partitioning of elements, leaving little room for other light elements, i.e., sulphur, carbon, and hydrogen (Wade and Wood, 2005; Siebert et al., 2013). Under equilibrium core formation processes, sulphur might be partitioned to the core, but the resulting amount in the core is expected to be no more than 2 wt.% (e.g., Boujibar et al., 2014). This implies that the core formation should have been processed under disequilibrium conditions if there is a larger amount of sulphur in the core.

The presence of sulphur in the core needs to be tested by Mineral Physics which includes establishing phase diagrams of relevant systems and measuring physical properties of candidate phases such as equation of state (EoS). The Fe-S system has shown a series of phase changes at relatively low pressures (Fei et al., 2000; Chen et al., 2008). Above 21 GPa the sulphide phase stable with Fe under subsolidus condition is Fe_3S which takes a tetragonal system (Fei et al, 2000) forming a simple eutectic system. The eutectic system between Fe and Fe_3S was recently examined under pressure by Mori et al. (2017), which confirmed the stability of Fe_3S to 250 GPa. As such the Fe_3S phase is stable over 200 GPa and constraining its physical properties provides vital information about a hypothetical sulphur-bearing core. The pressure-volume-temperature (*P*-*V*-*T*) or thermal EoS is a fundamental property when one considers the density profile of a core. In the present study, we focus on the *P*-*V*-*T* EoS of crystalline Fe_3S. The established EoS will also be of use to predict the nature of a breakdown reaction of Fe_3S at pressures above 250 GPa where tetragonal Fe_3S decomposes into an Fe-rich hexagonal close-packed (hcp) and S-rich cubic B2 phases (Ozawa et al. 2013). The breakdown of Fe_3S should change the eutectic relationship of the system Fe-S and the nature of the S-rich B2 phase needs to be clarified. The thermal EoS of Fe_3S will place tight constraints on the volume of the B2 phase by examining the volume change of the reaction. Moreover, a high-temperature compression curve of a solid phase can be the reference for estimating the properties of the counterpart liquid phase (Komabayashi, 2014). The first principles calculations predicted the density and velocity for Fe-S liquids under core pressures (Badro et al., 2014; Umemoto et al., 2014), which need to be tested by another approach. We will estimate the density of liquid Fe_3S under core pressures from the constructed EoS for solid Fe_3S.

72 The latest 300-K EoS for solid Fe_3S was reported by Kamada et al. (2014) based on
73 their compression data up to 200 GPa. In order to extrapolate their EoS to high temperature,
74 they employed a thermal pressure model:

75 $P(V,T) = P(V,300K) + P\text{th}\ (V,T)$……..(1)

76 where $P(V,T)$, $P(V,300K)$, and $P\text{th}\ (V,T)$ are the total pressure, pressure at 300 K at a given
77 sample volume, and thermal pressure at a given temperature. Kamada et al. (2014) adopted
78 the thermal pressure part proposed by Seagle et al. (2006) as

79 $P\text{th} = \alpha K_T*(T\text{-}300)$ ……..(2)

80 where α is the thermal expansion coefficient and K_T is the isothermal bulk modulus. The αK_T
81 value can be assumed to be constant above the Debye temperature. Therefore, a simple
82 relation of $\alpha K_T = \alpha_0 K_0$ holds for a material with low Debye temperature such as metals, where
83 the subscript 0 indicates at 1 bar and 300 K. Seagle et al. (2006) obtained a value of 0.011
84 GPa/K for $\alpha K_T = \alpha_0 K_0$. If K_0 for Fe_3S is assumed to range from 122.4 to 156 GPa (Seagle et
85 al., 2006; Kamada et al., 2014), the resulting α_0 would range from 7.05 to $8.99*10^{-5}$/K. This
86 α_0 value is however a factor of two larger compared to $3.84*10^{-5}$/K which was constrained by
87 low pressure experiments (Chen et al., 2007). Moreover, combining the 300-K parameters
88 and the thermal pressure parameters based on different pressure scales would not make a
89 consistent thermal EoS (Kamada et al., 2014). As such, a consistent thermal EoS of
90 crystalline Fe_3S needs to be precisely determined under simultaneous high *P*-*T* conditions.

91 In the present study, we collected the unit-cell volume data of crystalline Fe_3S under
92 simultaneous high-*P*-*T* conditions and constructed its thermal EoS. One of the challenges that
93 previous works encountered was the difficulty of synthesising single phase of crystalline Fe_3S
94 in the diamond anvil cell (DAC) when starting with a powder mixture of Fe and FeS (Seagle

et al., 2006; Kamada et al., 2012). In our experiments we used a flake with a composition of Fe_3S made by physical vapour deposition. It shows very homogeneous composition on the nanometre scale which enabled us to synthesise crystalline Fe_3S in the DAC. Based on the constructed thermal EoS, we will discuss the nature of a sulphur-rich core.

2. Experimental procedure

High pressures were generated in a DAC with a pair of opposed diamond anvils and rhenium gasket. The culet size of the diamond was 300 or 150 μm bevelled depending on the pressure range. The starting material was an amorphous metal flake with a composition of Fe_3S, produced by Dephis using a Physical Vapour Deposition technique. The flake was 3-4 μm thick and was homogeneous in composition on the nm scale (Morard et al., 2017) (Fig. S1). The starting material was sandwiched between layers of compressed pellets of KCl or SiO_2. The layer of KCl served as a pressure calibrant. Potassium chloride is known to show very low thermal expansivity and therefore can be used as a pressure marker even at high temperature by estimating the temperature gradient in the pressure medium (Dewaele et al., 2012; Tateno et al., 2019b). Runs where SiO_2 was used as a pressure medium also contained a pellet of $Fe_{0.93}O$ (McCammon and Liu, 1984) as a pressure calibrant, namely the sample and $Fe_{0.93}O$ layer were sandwiched between SiO_2 layers. Thanks to the double-sided heating by laser, the sample and $Fe_{0.93}O$ layer should be under the same temperature condition.

In-situ XRD experiments were performed at beamlines P02.2 at PETRA III (Liermann et al., 2015) and BL10XU at SPring-8 (Ohishi et al., 2008). Monochromatic X-rays of 0.2907 Å (P02.2) and 0.4134 Å (BL10XU) were focused on sample position with areas of 2*2 μm^2 (P02.2) and of approximately 6–μm full-width at half maximum (FWHM) (BL10XU). The experiments using KCl were performed at the P02.2 whereas the

119 experiments with SiO_2 and FeO were performed at the BL10XU. At both beamlines,
120 diffraction data were collected on flat panel detectors (Perkin Elmer XRD 1621 at P02.2 and
121 Perkin Elmer XRD 0822 at BL10XU), with an exposure time of 1 second. The diffraction
122 data were processed to conventional one-dimension patterns using software packages Dioptas
123 (Prescher and Prakapenka, 2015) and IPAnalyzer (Seto et al., 2010) for P02.2 and BL10XU
124 respectively.

125 High temperatures were generated with double-sided laser-heating systems at P02.2
126 and BL10XU. The diameter of the laser beam was about 20 μm. Temperatures were
127 measured with a spectroradiometric method. See Liermann et al. (2010) and Ohishi et al.
128 (2008) for details of the laser-heating setup at each beamline. As will be discussed later, the
129 temperatures for KCl were corrected as it was used as a pressure transmitting medium.

130 The samples were first compressed to target pressures at room temperature based on
131 the Raman shift of the diamond anvils (Akahama and Kawamura, 2004). The samples were
132 then heated to approximately 1500 K to crystallise solid Fe_3S from the amorphous starting
133 material. In-situ pressures were obtained from the lattice constants and the equation of state
134 for B2 KCl (Tateno et al., 2019b) or for B1 Fe_xO (Fischer et al., 2011). The EoS for Fe_xO by
135 Fischer et al. (2011) was constructed based on available experimental data with x ranging
136 from 0.94 to 0.955 which is fairly close to the x value in this study (0.93). In addition,
137 McCammon and Liu (1984) reported that the bulk modulus of Fe_xO is insensitive to the x
138 value when it is smaller than 0.96. Hereafter $Fe_{0.93}O$ will be referred to as FeO for simplicity.
139 The temperature was held until no further change was observed in the XRD pattern, ca. 10 to
140 15 minutes. The sample material was then further heated by increasing the laser power.
141 Diffraction patterns were repeatedly collected during each heating cycle. The samples were
142 then quenched by turning the laser power off.

3. Results

3.1. High-*P*-*T* experiments

We conducted six sets of heating cycles at 43 GPa to 126 GPa at two synchrotron beamlines. The sample unit-cell volume data were collected under high pressures at 4 room-*T* and 79 high-*T* conditions. The experimental *P*-*T* conditions and results are summarised in Fig. 1 and Table S1. Typical diffraction patterns are shown in Fig. 2, which demonstrate that single phase of Fe_3S was synthesised from the amorphous flake starting material. Both beamlines used double-sided laser heating with laser diameters of about 20 μm. A temperature distribution profile compared with X-ray position at BL10XU is shown in Fig. S2. As no other iron-alloy phases were observed, the sample was homogeneously composed of Fe_3S at least across the X-ray spot, ca. 6 μm.

At P02.2, four runs were conducted with the KCl pressure marker at 43 to 70 GPa. At the beginning of each run, the amorphous starting material was heated to 1500 K and the synthesis of crystalline Fe_3S was confirmed (Fig. 2). Diffraction lines of (002), (321), (112), (141), and (510) were used, when available, for the unit-cell volume calculations. At BL10XU, two runs were conducted with the FeO pressure marker at 118 to 126 GPa. We used diffraction lines (002), (321), (112), (420), (141), (222), (510), and (312), when applicable, for calculating the unit-cell volume of Fe_3S. In the 5^{th} run, a quenched XRD pattern only was collected after synthesising Fe_3S by laser.

In the runs at BL10XU, although Fe_3S and FeO layers were in contact, we consider that there have been no chemical reactions between those layers for the following reasons. (1) All the diffractions peaks were indexed with the expected phases (Fig. 2). (2) As will be

shown below, the unit-cell volumes of the Fe_3S phase at 300 K taken after heating cycles are consistent with the existing data, implying that the Fe_3S phase was not contaminated. (3) The pressures calculated from FeO and SiO_2 after heating cycle 6 (i.e., at 300 K) are 125.5 GPa (from one peak for FeO) and 120 ± 8 GPa (Grocholski et al., 2013), respectively, which are consistent. This implies that FeO was not contaminated. (4) Pommier et al. (2018) conducted high-*P*-*T* experiments in the system Fe-S-O and reported that FeO as a liquidus phase little accommodated S (up to 0.024 wt%) at 14 GPa and 1673 K, indicating that FeO can hardly be contaminated by sulphur even above the solidus temperature. As such, it is likely that no observable chemical contaminations took place in the Fe_3S and FeO phases.

For the calculation of the experimental pressures, the measured temperatures were adopted when employing an EoS of FeO as it was sandwiched between layers of SiO_2 and in contact with the sample and therefore it is expected that the FeO layer was under the same temperature condition as the sample. On the other hand, the temperatures for the KCl layers needed to be corrected following the method by Campbell et al. (2007) as KCl was used as a pressure medium and it was placed under a temperature gradient upon heating between high temperature (at the sample) and 300 K (in contact with diamond). Thanks to the very low thermal expansivity of KCl, the temperature difference would not yield a significant uncertainty in pressure (Table S1) (Dewaele et al., 2012; Tateno et al., 2019b).

The EoS proposed by Fischer et al. (2011) and Tateno et al. (2019b) were used for the pressure calculations with B1 FeO and B2 KCl respectively. The EoS for FeO was largely based on the EoS of Fe by Dewaele et al. (2006). The unit-cell volume of KCl at 300 K calculated with the EoS by Tateno et al. (2019b) is consistent with that of Dewaele et al. (2006) up to 60-70 GPa. Both EoS by Dewaele et al. (2006; 2012) were calibrated against Dorogokupets and Oganov (2007) and therefore the two pressure markers used in this study should give consistent pressures. As discussed below, the two datasets are consistent and

produce consistent EoS for Fe_3S and combining the two data sets collected at different pressure ranges (43-70 GPa and 118-126 GPa) enabled us to place tight constraints on the EoS parameters.

3.2. Room temperature EoS of Fe_3S

The obtained unit-cell volume data were used to establish an EoS for crystalline Fe_3S. For the room temperature data, the third-order Birch-Murnaghan EoS was employed:

$$P = \frac{3K_0}{2}\left[\left(\frac{V_0}{V}\right)^{7/3} - \left(\frac{V_0}{V}\right)^{5/3}\right]\left\{1 - \frac{3}{4}(4 - K')\left[\left(\frac{V_0}{V}\right)^{2/3} - 1\right]\right\} \quad \text{.....(2)}$$

where V_0 , K_0, and K' are the unit-cell volume, the bulk modulus and its pressure derivative at 1 bar and 300 K respectively. A least square fitting of our 300 K data yielded K_0 = 119 ± 19 GPa , K' = 5.6 ± 1.1 when V_0 was fixed at 377.0 $Å^3$ (Fei et al., 2000), which is fairly consistent with results of Seagle et al. (2006), Chen et al. (2007), and Kamada et al. (2014) (Table 1). Fig. 3 shows all these existing data together with our own. The pressure values in the existing datasets were recalculated based on consistent pressure scales (see Table 1). Since the parameters can be tightly constrained with a wide experimental pressure range, we fitted all the data listed above simultaneously, which yielded K_0 = 126 ± 2 GPa , K' = 5.1 ± 1 with V_0 fixed at 377.0 $Å^3$. A calculated compression curve is shown in Fig. 3 which agrees well with all the data. This is the reference line when we extended the EoS towards high temperature.

The presence of a magnetic transition in Fe_3S was discussed in the vicinity of 20 GPa at 300 K (Lin et al., 2004; Chen et al., 2007; Kamada et al., 2014). Although we did not collect the data below 43 GPa at 300 K, we made separate fittings of the available *P-V* data

up to 20 GPa and higher to examine how the magnetic transition may affect the EoS parameters. With fixing V_0 and K' at 377 Å^3 and 5.1, a fitting of the data below 20 GPa (Chen et al., 2007) yielded K_0 = 124 ± 8 GPa. Assuming the non-magnetic high-pressure phase would have different V_0 and K_0, a fitting of the data at greater pressures (Seagle et al., 2006; Chen et al., 2007; Kamada et al., 2014; this study) with fixing K' at 5.1 yielded V_0 = 377 ± 1 Å^3 and K_0 = 125 ± 2 GPa. As such there is no observable difference in the EoS between the two pressure ranges.

3.3. Thermal EoS of Fe_3S

The room-T EoS constructed above was extended to include high-T data with the thermal pressure model, equation (1). The thermal pressure part, Pth, was obtained with two different approaches: (i) the αK_T model and (ii) the Mie-Grüneisen Debye (MGD) model.

(i)A least square fitting to our high-T data yielded αK_T of 0.0035 ± 0.0001 GPa/K. From K_0 of 126 GPa, this gives $\alpha_0 = 2.7*10^{-5}$/K, which is slightly smaller than, but close to the experimental measurements made by Chen et al. (2007) of $\alpha_0 = 3.84*10^{-5}$/K, compared to $\alpha_0 = 7.1*10^{-5}$/K by Seagle et al. (2006). This confirms $\alpha K_T \sim \alpha_0 K_0$, which implies that 300 K is close to the Debye temperature.

(ii)In order to better understand the thermal properties of Fe_3S, we also employed the MGD model (Jackson and Rigden, 1996):

$$P\text{th} = \frac{\gamma}{V}\Delta E_{th}(\theta, T) \quad \text{.....(4)}$$

where γ is the Grüneisen parameter, ΔE_{th} is the change in thermal energy, and θ is the Debye temperature. The thermal energy was calculated from the Debye approximation:

$$Eth = \frac{9nRT}{(\theta/T)^3}\int_0^{\theta/T}\frac{\xi^3}{e^{\xi}-1}d\xi \quad \text{.....(5)}$$

where n, θ, and R are the number of atoms per formula unit, Debye temperature, and gas constant, respectively. The Debye temperature and Grüneisen parameter were assumed to be functions of the volume as:

$$\theta = \theta_0 \exp[(\gamma_0-\gamma)/q] \quad \text{.....(6)}$$

and

$$\gamma = \gamma_0 (V/V_0)^q \quad \text{.....(7)}$$

where θ_0, γ_0, and q are the Debye temperature, Grüneisen parameter at 1 bar and 300 K, and a dimensionless parameter.

As mentioned above, θ_0 is likely close to the room temperature. Assuming θ_0 for Fe_3S was the same as for pure iron of 417 K (Dewaele et al., 2006), a least square fitting of our high-T data yielded γ_0 = 0.9 ± 0.1 and q = 0.7 ± 0.5 (Table 1). This corresponds to α_0 = $2.3*10^{-5}$/K from the following equation,

$$\gamma = \alpha K_T V/\mathrm{Cv} \quad \text{.....(8)}$$

where C_v is the heat capacity at constant volume, which can be derived from the Debye model (e.g., Poirier, 2000). The value for q shows a large uncertainty which can make it to 1. In the case of q = 1, γ becomes a simple function of the volume in equation (7). Therefore, we made another fitting of the high-T data with q fixed at 1. The result yielded γ_0 = 1.01 ± 0.03 corresponding to $\alpha_0 = 2.6*10^{-5}$/K (Table 1). The derived α_0 value is close to the result of the fitting with the αK_T model of $2.7*10^{-5}$/K. Therefore, we consider γ = 1.01 ± 0.03 with q = 1 as the best-fit parameters. The results are listed in Table 1 and its compression curves are shown in Fig. 4.

257 Fig. 5 shows the misfit of the fitting with (a) the αK_T model and (b) MGD model. In
258 both fittings, most of the data points fall within ± 5 % and do not show clear pressure or
259 temperature dependence.

260

261 **4. Discussions**

262 4.1. Non-hydrostatic stress

263 The non-hydrostatic stress state inside the sample chamber could have affected the
264 unit-cell volume measurement. While the data with the KCl pressure medium would have
265 been less affected by the stress as KCl is a soft material and we conducted laser annealing
266 (Tateno et al., 2019b), the data with the FeO pressure marker and SiO_2 pressure medium
267 might have be more affected. Before heating cycle 6, the unit-cell volume of Fe_3S was 262.3
268 $Å^3$ at 122.4 GPa. The misfit of the volume to a 300 K EoS is 7.4 GPa which is fairly large. As
269 shown above, the 300 K EoS was well constrained by the literature and the large misfit is
270 likely due to the deviatoric stress. In addition, the unit-cell volume showed a large error of ±
271 1.7 $Å^3$ which is also due to the presence of the stress. Then, upon laser heating, the error
272 value was drastically reduced to ± 1.0 $Å^3$ at 1920 K (Table S1). The error did not improve
273 upon further heating to the highest temperature of 2530 K and remained almost constant to
274 the end of the heating cycle even after quenching. The misfit of the unit-cell volume of the
275 quenched Fe_3S phase was 2.5 GPa which is a reasonable value. As such, the high temperature
276 laser annealing practically released the deviatoric stress and the remaining stress inside the
277 sample chamber should have been minimal as we did not see further reduction in the error of
278 the unit-cell volume of Fe_3S when we increased the laser power. Those high-T and quenched
279 data were used for the fitting to the EoS (Table S1).

280

281 4.2.Thermal EoS of crystalline Fe_3S

282 The pressures in our experiments were calibrated against the consistent pressure
283 scales of KCl and FeO as discussed above. Both scales were based on a self-consistent set of
284 scales by Dorogokupets and Oganov (2007). In the 300 K fitting for Fe_3S, we also used data
285 by Seagle et al. (2006), Chen et al. (2007), and Kamada et al. (2014), all of which were based
286 on a set of pressure scales by Fei et al. (2007) (Table 1). At 300 K, Fei et al. (2007)'s scales
287 are consistent with the EoS of Fe by Dewaele et al. (2006) which was calibrated against
288 Dorogokupets and Oganov (2007) (Fei et al., 2016). In summary, the EoS for Fe_3S we
289 propose here was constructed based on the consistent pressure scales.

290 Table 1 lists the high-temperature parameters of this study with those of existing
291 literatures. As mentioned above, the αK_T value of this study implies $\alpha K_T = \alpha_0 K_0$, which is
292 consistent with the low Debye temperature common to the metals. As such, the parameters
293 set established in this study provides a more consistent and reasonable thermal EoS for
294 crystalline Fe_3S. Our αK_T value is significantly smaller than that in Seagle et al. (2006),
295 which leads to a denser Fe_3S phase. Here we consider two major sources for the discrepancy
296 in the αK_T term: (1) the 300 K compression curve by Seagle et al. (2006) and (2) the pressure
297 scale. (1) Seagle et al. (2006) obtained the 300 K EoS parameters for Fe_3S against an EoS for
298 Fe mixed with Fe_3S. However, as they pointed out themselves thus-obtained 300 K EoS for
299 Fe_3S was not consistent with their another one based on a NaCl EoS. NaCl which served as a
300 pressure medium is much softer than Fe, so that it should have been under better hydrostatic
301 conditions and produced more reliable sample pressure values. As a matter of fact, the NaCl
302 pressure values (recalculated in this study, see Table 1) are consistent with other existing
303 studies (Chen et al., 2007; Kamada et al., 2014; this study) and used for our 300 K EoS fitting

(Fig. 3). As such their unit-cell volumes of Fe at 300 K might not be reliable. (2) The pressure values of their high-temperature data were recalculated using Dewaele et al. (2006)'s EoS for Fe to be consistent with our 300 K compression curve. Then we fitted those high-T data to the αK_T term, yielding αK_T = 0.0060 GPa/K which was significantly reduced from their original value of 0.011 GPa/K. The above considerations partially solve the discrepancy between Seagle et al. (2006) and this study.

The thermal pressure term for a metal may include additional terms under the core temperatures, ca. 4000-6000 K, namely the anharmonic term and electronic term (e.g., Alfè et al., 2001). If a material shows significant contributions from the anharmonic and electronic terms, the αK_T value should show a positive temperature dependence (Alfè et al., 2001). Fig. 5a shows the misfit of the fitting with a single αK_T value of 0.0035 GPa/K and there is no clear temperature dependence up to the highest temperature studied here. Note that runs at BL10XU at 118-126 GPa may seem to show a weak temperature dependence (Fig. 5a). However this should not be caused by either the anharmonic or electronic contribution as those terms would be more pronounced under lower compression at the same temperature (Dewaele et al., 2006) and the runs at P02.2 at 43-70 GPa clearly show no temperature dependence. Therefore, solid Fe_3S would show negligible contributions from the anharmonic and electronic terms. As such the MGD model with only the vibrational term would suffice for examining the density of the phase even under the core temperature conditions.

Fig. 6 compares compression curves of various iron alloys (Fe, Dewaele et al., 2006; Fe_3S, this study; Fe_3C, FeSi, FeS VI, and FeS VII, Sata et al., 2010; Fe-9wt%Si hcp Fe, Tateno et al., 2015; FeO B1, Fischer et al., 2011). Fe_3S shows almost the same average atomic volume as Fe under core pressures. Table 2 shows selected physical properties of pure Fe and Fe_3S under core P-T conditions calculated from the EoS (Dewaele et al., 2006; this

328 study). The volume difference between the phases is a little enhanced at 5500 K because of
329 the negligible anharmonic and electronic terms in the thermal pressure term in Fe_3S.

330

331 4.3. The nature of the high-pressure breakdown reaction of Fe_3S

332 Solid Fe_3S is stable to 250 GPa and undergoes a decomposition reaction into an Fe-
333 rich hcp phase and a S-rich B2 phase at a higher pressure (Ozawa et al., 2013), which should
334 modify the eutectic relationship of the system Fe-S. The nature of the reaction of Fe_3S = Fe-
335 rich hcp + S-rich B2 however was not well understood. Here we examine properties of the B2
336 phase, assuming the composition of the hcp phase is pure Fe. Ozawa et al. (2013) reported
337 the lower bound for the sulphur content of the B2 phase was 33.5 atm% which is close to
338 Fe_2S. We therefore tentatively assume the composition of the B2 phase is Fe_2S. As such the
339 discussions below will provide a case for the B2 phase with the least possible sulphur content,
340 although the detailed analyses of the chemical composition of the phase should be made in
341 the future.

342 Fig. 7a plots the average atomic volumes for Fe and Fe_3S at 250 GPa and 300 K,
343 based on which the volume for Fe_2S is estimated. The laws of thermodynamics require that
344 the average atomic volume for the B2 phase needs to be below the Fe-Fe_3S line (Fig. 7a),
345 because a first-order pressure-induced transition must be accompanied with a volume
346 reduction. We here consider two possible cases: (i) the volume change of the reaction (ΔVr)
347 of Fe_3S = Fe + Fe_2S is zero, and (ii) ΔVr = -1.5%. The volume for Fe_2S is then obtained for
348 each case in Fig. 7a. Employing the same calculations at different pressures produces
349 compression curves for Fe_2S (Fig. 7b) with the parameters, V_0 = 11.963 Å^3/atom, K_0 = 115.0
350 GPa, and K' = 5.18 for ΔVr = 0, and V_0 = 11.729 Å^3/atom, K_0 = 114.8 GPa, and K' = 5.18 for
351 ΔVr = -1.5%. Since the volumes of Fe_3S and Fe are similar at 300 K, the resulting volume of

352 Fe_2S is not very sensitive to the ΔVr value (Fig. 7b) and therefore, the predicted compression
353 behaviour here would be fairly reliable. Very recently Tateno et al. (2019a) has reported
354 experimental data on the unit-cell volume of the Fe_2S phase at pressures greater than 180 GPa.
355 Their volume of Fe_2S is plotted in Fig. 7a, with the pressure values corrected to be consistent
356 with the pressure scale in this study. Their data shows 1.0 % volume reduction on the
357 breakdown reaction of $Fe_3S = Fe+Fe_2S$, which is within our prediction (0-1.5%). Any future
358 measurements of the volume of the S-rich B2 phase should be compared with the curves in
359 Fig. 7b.

360

361 4.3. Sulphur in the Earth's core

362 Fig. 8a shows density profiles of solid Fe_3S from the EoS established in this study at
363 300, 4000, and 5500 K compared with a seismologically constrained density model (PREM,
364 Dziewonski and Anderson, 1981) over the core pressure range. Isothermal compression
365 curves at 4000 and 5000 K from Kamada et al. (2014) are also plotted. Our EoS calculates
366 the density of solid Fe_3S greater than Kamada et al. (2014)'s EoS since Kamada et al. (2014)
367 included the large αK_T value proposed by Seagle et al. (2006). At 330 GPa and 5500 K which
368 is a relevant condition to the inner core-outer core boundary (ICB), our Fe_3S is 2.9 % denser
369 than Kamada et al. (2014)'s.

370 The density of solid Fe_3S at 300 K is calculated to be smaller than the inner core
371 PREM (Fig. 8a). As the compression behaviour of Fe_3S at 300 K is well constrained to 200
372 GPa (Seagle et al., 2006; Chen et al., 2007; Kamada et al., 2014; this study), the uncertainty
373 of the calculated unit-cell volume when extrapolated to 330 GPa is ± 0.2 %. This ensures that
374 solid Fe_3S is less dense than the inner core at core temperatures due to thermal expansion.

We here estimate the density profile of liquid Fe_3S. As discussed above, the average atomic volume is similar between Fe and Fe_3S under the core pressure conditions (Fig. 6), which means that replacing an Fe atom for a S atom would little change the volume of the alloy although the structure is slightly distorted from hcp to tetragonal. This suggests that other physical properties of Fe_3S could also be more similar to those of Fe compared with the other Fe-light element alloys. We therefore assume ΔV upon melting (ΔVm) for Fe_3S to be the same as for pure iron under core pressures (Table 2). It is expected that the temperature profile over the outer core would be adiabatic due to the convection. However, since the Grüneisen parameter for liquid Fe_3S is not available, we assume a temperature gradient by 1500 K through the outer core, i.e, 4000 K at 140 GPa and 5500 K at 330 GPa. This temperature gradient is consistent with pure Fe with a Grüneisen parameter of about 1.5 (Vočadlo et al., 2003; Komabayashi, 2014). Thus-calculated density profile for liquid Fe_3S matches the outer core density within an uncertainty of 1 % (Fig. 8b). This discussion is more sensitive to ΔVm than the value of the adiabatic temperature gradient over the outer core, namely, under any reasonable core temperatures (4000-6000 K). The sulphur content in the outer core needs to be as much as 16 wt% (Fe_3S) if it is the sole light element in the core.

Our data for the liquid density is compared with existing first principles calculations (Badro et al., 2014; Umemoto et al., 2014). We adopted Badro et al. (2014)'s sulphur concentration dependence of the density of iron liquid (Komabayashi, 2014) and found that Fe-12 wt%S at 6300 K and Fe-10 wt%S at 4300 K could match the PREM values at 330 GPa and 135 GPa respectively. Umemoto et al. (2014) calculated the density of Fe_3S liquid along an isentrope with 5400 K at 330 GPa. The data of Umemoto et al. (2014) and this study were obtained at similar temperature ranges and the results are fairly consistent (Fig. 8b). The amount of a light element required for the PREM density increases with reducing the core temperature, and therefore, the results of Badro et al. (2014) can be qualitatively consistent

400 with ours. However, for more precise comparison, the temperature dependence of the liquid
401 density needs to be clarified in the future.

402 The eutectic composition in the system Fe-Fe_3S was reported to become close to the
403 Fe side with increasing pressure (Mori et al., 2017). At 250 GPa, it would be about 6 wt%S,
404 which means a S-richer liquid crystallises Fe_3S at liquidus. On the other hand, as we
405 discussed above, crystalline Fe_3S is not stable in the inner core as it breaks down to the
406 mixture of Fe-rich hcp phase and S-rich B2 phase above 250 GPa (Ozawa et al., 2013). This
407 results in a formation of the S-rich B2 phase from a liquid with S > 6wt% at ICB at 330 GPa.
408 Assuming that the B2 phase has a composition of Fe_2S and causes ΔVr = 0 ~ -1.5 % as
409 discussed above (Fig. 7a), the density profile of B2 Fe_2S for the inner core range is calculated
410 along a 5500 K isotherm (Fig. 8b). The density of Fe_2S is likely less dense than solid Fe_3S
411 and cannot match the inner core density. As such, the liquidus phase at Fe-16wt%S (Fe_3S) is
412 not the constituent phase of the inner core. In summary, while the outer core density requires
413 as much sulphur as 16 wt%, the resulting liquidus phase cannot meet the density of the inner
414 core. We therefore suggest that any sulphur-rich iron composition should be rejected for the
415 Earth's core. Nevertheless, this does not exclude the possibility of sulphur in the core. If the
416 sulphur content in the outer core is less than 6 wt%, the crystallising liquidus phase at the
417 ICB would be an Fe-rich hcp phase which can match the density of the inner core (Mori et al.,
418 2017), although this requires the presence of other light elements in the outer core. Metal-
419 silicate partitioning experiments under high pressure demonstrated that sulphur can be
420 partitioned into core melt up to 2 wt% (e.g., Boujibar et al., 2014), which is smaller than 6
421 wt% for the eutectic composition (Mori et al., 2017). If the amount of sulphur in Earth's core
422 is between 2 and 6 wt%, the core formation process might have been, at least partly,
423 processed under disequilibrium conditions.

424

5. Conclusions and future perspective

A new thermal EoS for crystalline Fe_3S has been established based on 83 new experimental *P-V-T* data together with the existing 300-K data. A constant αK_T value well fits the high-*T* data to the highest experimental temperature, which implies that the contributions from the anharmonic and electronic terms would be minor in the thermal pressure term. The average atomic volume of Fe_3S is similar to that of pure Fe under the core pressures. The density of crystalline Fe_3S is greater than of the Earth's outer core, and assuming a density reduction due to melting, liquid Fe_3S would match the outer core density profile within the uncertainty of 1 %. However, the volume of Fe_2S B2 phase which is assumed to be a breakdown product of Fe_3S above 250 GPa is likely less dense than Fe_3S and does not match the PREM model in the inner core. An S-rich bulk (e.g., Fe_3S) composition would crystallise the less dense S-rich B2 phase upon entering the inner core conditions. Therefore, any S-rich outer core is rejected for the Earth.

The above discussions can be applicable to other terrestrial planetary cores, such as Martian core, which properties may be explored by seismometers deployed by the InSight mission (Banerdt et al., 2013). The pressure conditions for its iron-rich core were estimated to be 19-38 GPa and it may contain sulphur of 11-17 wt% (Helffrich, 2017). The eutectic compositions should be between Fe and Fe_3S and therefore the liquidus phase, i.e., the constituent of a solid core (if any) would be Fe_3S phases. The data presented in this study will provide the key information to interpret the seismological data by the InSight mission.

The current limitations include that there are no experimental data reported on the velocity of the Fe-S liquids under core pressures. A promising approach is the construction of a self-consistent thermodynamic model based on experimental data (e.g., melting temperatures, EoS for solid phases) to derive the EoS of the liquid phase, which allows us to

449 calculate the liquid velocity as well as density (Komabayashi, 2014). A further comparison of
450 the liquid properties between experimentally-derived model and the first principles
451 calculations will bring us a better understanding of the planetary cores' properties.

452

453 **Acknowledgements**

454 We acknowledge DESY (Hamburg, Germany), a member of the Helmholtz Association HGF,
455 for the provision of experimental facilities (proposal no. I-20160586 EC; I-20170740 EC).
456 Parts of this research were carried out at PETRA III. DESY also financially supports our visit
457 to the beamline. SPring-8 (Hyogo, Japan) is also acknowledged for the provision of
458 experimental facilities at BL10XU (proposal no. 2017B1338). Two anonymous reviewers are
459 acknowledged for their constructive comments which improved the quality of the paper. This
460 research was supported by the European Research Council (ERC) Consolidator Grant to TK
461 (Earth core #647723).

462 **References**

463 Akahama, Y., Kawamura, H., 2004. High-pressure Raman spectroscopy of diamond anvils to
464 250 GPa: Method for pressure determination in the multimegabar pressure range. J.
465 Appl. Phys. 96, 3748-3751.

466 Alfè, D., Price, G.D., Gillan, M.J., 2001. Thermodynamics of hexagonal-close-packed iron
467 under Earth's core conditions. Phys. Rev. B 64, 045123.

468 Badro, J., Cote, A.S., Brodholt, J.P., 2014. A seismologically consistent compositional model
469 of Earth's core. Proc. Natl. Acad. Sci. U. S. A. 111, 7542-7545.
470 Doi/10.1073/pnas.1316708111.

471 Banerdt, W., Smrekar, S., Lognonné, P., Spohn, T., Asmar, S., Banfield, D., Boschi, L.,
472 Christensen, U., Dehant, V., Folkner, W., Giardini, D., Goetze, W., Golombek, M.,
473 Grott, M., Hudson, T., Johnson, C., Kargl, G., Kobayashi, N., Maki, J., Mimoun, D.,
474 Mocquet, A., Morgan, P., Panning, M., Pike, W., Tromp, J., van Zoest, T., Weber, R.,
475 Wieczorek, M., Garcia, R., Hurst, K., 2013. InSight: a discovery mission to explore
476 the interior of Mars., 44th Lunar and Planetary Science, Conference, Houston, p. 1915.

477 Birch, F., 1952. Elasticity and constitution of the Earth's interior. J. Geophys. Res. 57, 227–
478 286.

479 Boujibar, A., Andrault, D., Bouhifd, M.A., Bolfan-Casanovaa, N., Devidal, J.-L., Trcera, N.,
480 2014. Metal-silicate partitioning of sulphur, new experimental and thermodynmaic
481 constraints on planetary accretion. Earth Planet. Sci. Lett. 391, 42-54.

482 Campbell, A.J., Seagle, C.T., Heinz, D.L., Shen, G., Prakapenka, V.B., 2007. Partial melting
483 in the iron-sulfur system at high pressure: A synchrotron X-ray diffraction study. Phys.
484 Earth Planet. Inter. 162, 119–128.

485 Chen, B., Gao, L., Funakoshi, K., Li, J., 2007. Thermal expansion of iron-rich alloys and
486 implications for the Earth's core. Proc. Natl. Acad. Sci. U. S. A. 104, 9162–9167.

487 Chen, B., Li, J., Hauck, S.A., 2008. Non-ideal liquidus curve in the Fe-S system and
488 Mercury's snowing core. Geophys. Res. Lett. 35.

489 Dewaele, A., Belonoshko, A.B., Garbarino, G., Occelli, F., Bouvier, P., Hanfland, M.,
490 Mezouar, M., 2012. High-pressure-high-temperature equation of state of KCl and KBr.
491 Phys. Rev. B Phys. 85, 1–7.

492 Dewaele, A., Loubeyre, P., Occelli, F., Mezouar, M., Dorogokupets, P.I., Torrent, M., 2006.
493 Quasihydrostatic equation of state of Iron above 2 Mbar. Phys. Rev. Lett. 97, 29–32.

494 Dorogokupets, P.I., Oganov, A.R., 2007. Ruby, metals, and MgO as alternative pressure
495 scales: a semiemprical description of shock-wave, ultrasonic, x-ray, and
496 thermochemical data at high temperatures and pressures. Phys. Rev. B 75, 024115.

497 Dziewonski, A.M., Anderson, D.L., 1981. Preliminary reference Earth model. Phys. Earth
498 Planet. Inter. 25, 297-356.

499 Fei, Y., LI, J., BERTKA, C.M., PREWITT, C.T., 2000. Structure type and bulk modulus of
500 Fe 3 S , a new iron-sulfur compound. Am. Mineral. 85, 1830–1833.

501 Fei, Y., Ricolleau, A., Frank, M., Mibe, K., Shen, G., Prakapenka, V., 2007. Toward an
502 internally consistent pressure scale. Proc. Natl. Acad. Sci. U. S. A. doi:
503 10.1073/pnas.0609013104.

504 Fei, Y., Murphy, C., Shibazaki, Y., Shahar, A., Huang, H., 2016. Thermal equation of state of
505 hcp-iron: constraint on the density deficit of Earth's solid inner core. Geophy. Res.
506 Lett. 43, 6837-6843.

507 Fischer, R.A., Campbell, A.J., Shofner, G.A., Lord, O.T., Dera, P., Prakapenka, V.B., 2011.
508 Equation of state and phase diagram of FeO. Earth Planet. Sci. Lett. 304, 496–502.

509 Goldstein, J.I., Scott, E.R.D., Chabot, N.L., 2009. Iron meteorites: Crystallization, thermal
510 history, parent bodies, and origin. Chemie der Erde 69, 293–325.

511 Grocholski, B., Shim, S.H., Prakapenka, V.B., 2013. Stability, metastability, and elastic
512 properties of a dense silica polymorph, seifertite. J Geophys Res-Solid Earrth 118,
513 4745-4757.

514 Helffrich, G., 2017. Mars core structure-concise review and anticipated insights from InSight.
515 Prog. Earth Planet. Sci. 4(24), doi: 10.1186/s40645-017-0139-4.

516 Hirose, K., Labrosse, S., Hernlund, J., 2013. Composition and State of the Core. Annu. Rev.
517 Earth Planet. Sci. 41, 657–691.

518 Jackson, I., Rigden, S.M., 1996. Analysis of P-V-T data: constraints on the thermoelastic
519 properties of high-pressure minerals. Phys. Earth Planet. Inter. 96, 85-112.

520 Kamada, S., Ohtani, E., Terasaki, H., Sakai, T., Miyahara, M., Ohishi, Y., Hirao, N., 2012.
521 Melting relationships in the Fe-Fe_3S system up to the outer core conditions. Earth
522 Planet. Sci. Lett. 359–360, 26–33.

523 Kamada, S., Ohtani, E., Terasaki, H., Sakai, T., Takahashi, S., Hirao, N., Ohishi, Y., 2014.
524 Equation of state of Fe3S at room temperature up to 2megabars. Phys. Earth Planet.
525 Inter. 228, 106–113.

526 Komabayashi, T., 2014. Thermodynamics of melting relations in the system Fe-FeO at high
527 pressure: Implications for oxygen in the Earth's core. J. Geophys. Res. Solid Earth
528 4164–4177.

529 Liermann, H-P., Morgenroth, W., Ehnes, A., Berghauser, A., Winkler, B., Franz, H., Weckert,
530 E., 2010. The extreme conditions beamline at PETRA III, DESY: possibilities to
531 conduct time resolved monochromatic diffraction experiments in dynamic and laser
532 heated DAC. J. Phys. Conf. Ser. 215, 012029, doi:10.1088/1742-6596/215/1/012029.

533 Lin, J.F., Fei, Y., Sturhahn, W., Zhao, J., Mao, H., Hemley, R.J., 2004. Magnetic transition
534 and sound velocities of Fe_3S at high pressure: implications for Earth and planetary
535 cores. Earth Planet. Sci. Lett. 226, 33-40.

536 Mccammon, C.A., Liu, L.G., 1984. The Effects of Pressure and Temperature on
537 Nonstoichiometric Wustite, FexO -the Iron-Rich Phase-Boundary. Phys. Chem.
538 Mineral 10, 106-113.

539 McDonough, W.F., Sun, S. s., 1995. The composition of the Earth, in: Chemical Geology. pp.
540 223–253.

541 Morard, G., Andrault, D., Antonangeli, D., Nakajima, Y., Auzende, A.L., Boulard, E.,
542 Cervera, S., Clark, A., Lord, O.T., Siebert, J., Svitlyk, V., Garbarino, G., Mezouar, M.,
543 2017. Fe-FeO and Fe-Fe_3C melting relations at Earth's core-mantle boundary
544 conditions: Implications for a volatile-rich or oxygen-rich core. Earth Planet. Sci. Lett.
545 473, 94-103.

546 Mori, Y., Ozawa, H., Hirose, K., Sinmyo, R., Tateno, S., Morard, G., Ohishi, Y., 2017.
547 Melting experiments on Fe–Fe3S system to 254 GPa. Earth Planet. Sci. Lett. 464,
548 135–141.

549 Ohishi, Y., Hirao, N., Sata, N., Hirose, K., Takata, M., 2008. Highly intense monochromatic
550 X-ray diffraction facility for high-pressure research at SPring-8. High Press. Res. 28,
551 163–173.

552 Ozawa, H., Hirose, K., Suzuki, T., Ohishi, Y., Hirao, N., 2013. Decomposition of Fe_3S above
553 250 GPa. Geophys. Res. Lett. 40, 4845–4849.

554 Palme, H., O'Neill, H., 2003. Cosmochemical Estimates of Mantle Composition. Treatise
555 Geochemistry Second Ed. 3, 1–39.

556 Poirier, J.P., 1994. Light elements in the Earth's outer core: A critical review. Phys. Earth
557 Planet. Inter. 85, 319–337.

558 Poirier, J.P., 2000. Introduction to the Physics of the Earth's Interior, 2nd ed. Cambridge Univ.
559 Press. 312pp.

560 Pommier, A., Laurenz, V., Davies, C.J., Frost, D.J., 2018. Melting phase relations in the Fe-S
561 and Fe-S-O systems at core conditions in small terrestrial bodies. Icarus 306, 150-162.

562 Prescher, C., Prakapenka, V.B., 2015. DIOPTAS: A program for reduction of two-
563 dimensional X-ray diffraction data and data exploration. High Press. Res. 35, 223–
564 230.

565 Sata, N., Hirose, K., Shen, G., Nakajima, Y., Ohishi, Y., Hirao, N., 2010. Compression of
566 FeSi, Fe_3C, $Fe_{0.95}O$, and FeS under the core pressures and implication for light
567 element in the Earth's core. J. Geophys. Res. 115, B09204,
568 doi:09210.01029/02009JB006975.

569 Seagle, C.T., Campbell, A.J., Heinz, D.L., Shen, G., Prakapenka, V.B., 2006. Thermal
570 equation of State of Fe_3S and implications for sulfur in Earth's core. J. Geophys. Res.
571 Solid Earth 111, 1–7.

572 Seto, Y., Nishio-Hamane, D., Nagai, T., Sata, N., 2010. Development of a Software Suite on
573 X-ray Diffraction Experiments. Rev. High Press. Sci. Technol. 20, 269–276.

574 Siebert, J., Badro, J., Antonangeli, D., Ryerson, F.J., 2013. Terrestrial accretion under
575 oxidizing conditions. Science 339, 1194-1197.

576 Tateno, S., Kuwayama, Y., Hirose, K., Ohishi, Y., 2015. The structure of Fe-Si alloy in
577 Earth's inner core. Earth Planet. Sci. Lett. 418, 11-19.

578 Tateno, S., Ozawa, H., Hirose, K., Suzuki, T., Kawaguchi, S.I., Hirao, N., 2019a. Fe_2S: The
579 most Fe-rich iron sulfide at the Earth's inner core pressures. Geophys. Res. Lett.
580 10.1029/2019GL085248.

581 Tateno, S., Komabayashi, T., Hirose, K., Hirao, N., Ohishi, Y., 2019b. Static compression of
582 B2 KCl to 230 GPa and its *P-V-T* equation of state. Am. Mineral. 104, 718-723.

583 Umemoto, K., Hirose, K., Imada, S., Nakajima, Y., Komabayashi, T., Tsutsui, S., Baron,
584 A.Q.R., 2014. Liquid iron-sulfur alloys at outer core conditions by first-principles
585 calculations. Geophys. Res. Lett. 41, 6712-6717. Doi:10.1002/2014GL061233.

586 Vočadlo, L., Alfé, D., Gillan, M.J., Price, G.D., 2003. The properties of iron under core
587 conditions from first principles calculations. Phys. Earth Planet. Inter. 140, 101–125.

588 Wade, J., Wood, B.J., 2005. Core formation and the oxidation state of the Earth. Earth Planet.
589 Sci. Lett. 236, 78-95.

590 Williams, H.M., Markowski, A., Quitté, G., Halliday, A.N., Teutsch, N., Levasseur, S., 2006.
591 Fe isotope fractionation in iron meteorites: New insights into metal-sulphide
592 segregation and planetary accretion. Earth Planet. Sci. Lett. 250, 486–500.

593

594

595

596 **Figure captions**

597 Figure 1. Experimental *P-T* conditions of this study and selected existing reports (Seagle et
598 al., 2006; Chen et al., 2007; Kamada et al., 2014; this study). The pressures in this study were
599 based on the EoS of FeO (Fischer et al., 2011) and KCl (Tateno et al., 2019b). The pressures
600 in Seagle et al. (2006) at 300 K and Chen et al. (2007) were recalculated; see Table 1.

601

602 Figure 2. Representative XRD patterns with KCl pressure marker collected at P02.2 (top) and
603 with FeO pressure marker at BL10 XU (bottom).

604

605 Figure 3. Unit-cell volumes for Fe_3S at 300 K (Seagle et al., 2006; Chen et al., 2007; Kamada
606 et al., 2014; this study). A compression curve fitted to all the data is also shown. The
607 parameters set for the EoS is given in Table 1.

608

609 Figure 4. Unit-cell volumes for Fe_3S under high temperatures collected in this study.
610 Compression curves based on the thermal EoS constructed in this study are shown together
611 with those by Kamada et al. (2014).

612

613 Figure 5. Misfit of high-temperature data to the EoS with the αK_T model and MGD model.

614

615 Figure 6. Comparison of compression curves of different iron alloys at 300 K. Data sources
616 are Fe, Dewaele et al. (2006); Fe_3S, this study; Fe-9wt%Si, Tateno et al. (2015); FeSi, Fe_3C,

617 FeS VI and FeS VII, Sata et al. (2010); FeO, Fischer et al. (2011). The average atomic
618 volumes of Fe and Fe_3S are similar under the core pressures. CMB, core-mantle boundary.

619

620 Figure 7. (a) Volume relationships for the reaction Fe_3S = Fe-rich hcp phase + S-rich B2
621 phase (Ozawa et al., 2013). The composition of the hcp phase is assumed to be pure Fe. The
622 volumes were calculated from Dewaele (2006) for Fe and this study for Fe_3S. The star
623 represents a hypothetical B2 phase with a composition of Fe_2S (Ozawa et al., 2013). The
624 volumes of the hypothetical Fe_2S phase was estimated for the cases of ΔVr = 0 and -1.5%
625 respectively. The open square indicates the volume of Fe_2S constrained by experiment
626 (Tateno et al., 2019a) with the pressure value recalculated based on Dorogokupets and
627 Oganov (2007). (b) Compression curves of the hypothetical Fe_2S at 300 K.

628

629 Figure 8. (a) Isothermal density profiles of solid Fe_3S based on this study at 300 (black
630 dashed), 4000 (black solid), and 5000 K (green solid), compared with those at 4000 and 5000
631 K by Kamada et al. (2014). For reference, a compression profile of hcp Fe (Dewaele et al.,
632 2006) along a 5500 K isotherm and the seismologically constrained density profiles (PREM,
633 Dziewonski and Anderson, 1981) are also plotted. Due to the low thermal expansivity, the
634 EoS of this study produces a denser Fe_3S profile than of Kamada et al. (2014). (b) Density of
635 liquid Fe_3S estimated from the solid phase EoS along an isentrope starting with 5500 K at the
636 ICB (red). An isentropic density profile of liquid Fe is also shown (dashed line, Komabayashi,
637 2014) starting with 6400 K at ICB which is the liquidus temperature. Results from the first
638 principles calculations are also shown (blue line for Fe_3S along an isentrope with 5400 K at
639 ICB, Umemoto et al., 2014; squares for Fe-10wt%S at 4300 K, and for Fe-12wt%S at 6300 K,
640 modified after Badro et al., 2014). Note that we adopted Badro et al. (2014)'s sulphur

concentration dependence of the density of iron liquid (Komabayashi, 2014) for the squares. An estimated density range of Fe_2S B2 phase for the inner core range at 5500 K is shown: the lower and upper bounds are for $\Delta Vr = 0$ and -1.5% respectively.

Table 1. Parameters for equation of state for crystalline Fe_3S

	V_0 (Å^3)	K_0 (GPa)	K'	γ_0	q	θ_0 (K)	$\alpha_0 K_0$ (GPa K^{-1})	α_0 (*10^{-5} K^{-1})	Ref
Room-T	377.0(2)	170(8)	2.6(5)	-	-	-	-	-	Fei et al. (2000)
	377.0 (fixed)	156(7)	3.8(3)	-	-	-	-	-	Seagle et al. (2006)
	377.0 (fixed)	136(5)	4.2(3)	-	-	-	-	-	Seagle et al. (2006)[a]
	377.0 (fixed)	134(11)	5.1(10)	-	-	-	-	-	Chen et al. (2007)
	377.0 (fixed)	125.3(1.7)	5.1(1)	-	-	-	-	-	Kamada et al. (2014)
	377.0 (fixed)	119(19)	5.6(1.1)	-	-	-	-	-	This study
	377.0 (fixed)	126(2)	5.1(1)	-	-	-	-	-	This study, Seagle et al. (2006)[a], Chen et al. (2007)[b], Kamada et al. (2014)
High-T	377.0 (fixed)	113 (fixed)	5.2 (fixed)	-	-	-	0.011(2)	7.1[c]	Seagle et al. (2006)[d]
				-	-	-	-	3.84	Chen et al. (2007)
	377.0 (fixed)	126 (fixed)	5.1(fixed)	-	-	-	0.0035(1)	2.7[c]	This study
	377.0 (fixed)	126 (fixed)	5.1(fixed)	0.9(1)	0.6(5)	417 (fixed)		2.3[e]	This study
	377.0 (fixed)	126 (fixed)	5.1(fixed)	1.01(3)	1(fixed)	417 (fixed)		2.6[e]	This study

[a] The experimental pressure values were recalculated based on NaCl-B2 by Fei et al. (2007)

[b] The experimental pressure values were recalculated based on Au by Fei et al. (2007)

[c] α_0 was calculated from the $\alpha_0 K_0$ and K_0 values.

[d] The EoS was calibrated against a thermal EoS of hcp Fe.

[e] α_0 was calculated from equation (8) and γ_0 value.

Table 2. Physical properties of Fe_3S and Fe

		300 K			*5500 K*			
		ρ (g/cm^3)	V (Å^3/atom)	K_T (GPa)	ρ (g/cm^3)	V (Å^3/atom)	K_T (GPa)	$\triangle V$ *on melting* (Å^3/atom)
Fe_3S	140 GPa	10.48	7.907	715	10.20	8.123	643	
	250 GPa	11.83	7.004	1132	11.63	7.122	1063	
	330 GPa	12.60	6.577	1427	12.43	6.664	1360	
Fe (hcp)[a]	140 GPa	11.73	7.908	745	10.76	8.615	550	0.21
	250 GPa	13.21	7.022	1130	12.50	7.420	954	0.16
	330 GPa	14.07	6.589	1394	13.46	6.892	1225	0.14

[a] Fe properties are calculated from the EoS by Dewaele et a. (2006) except for $\triangle V$ on melting (Komabayashi 2014).

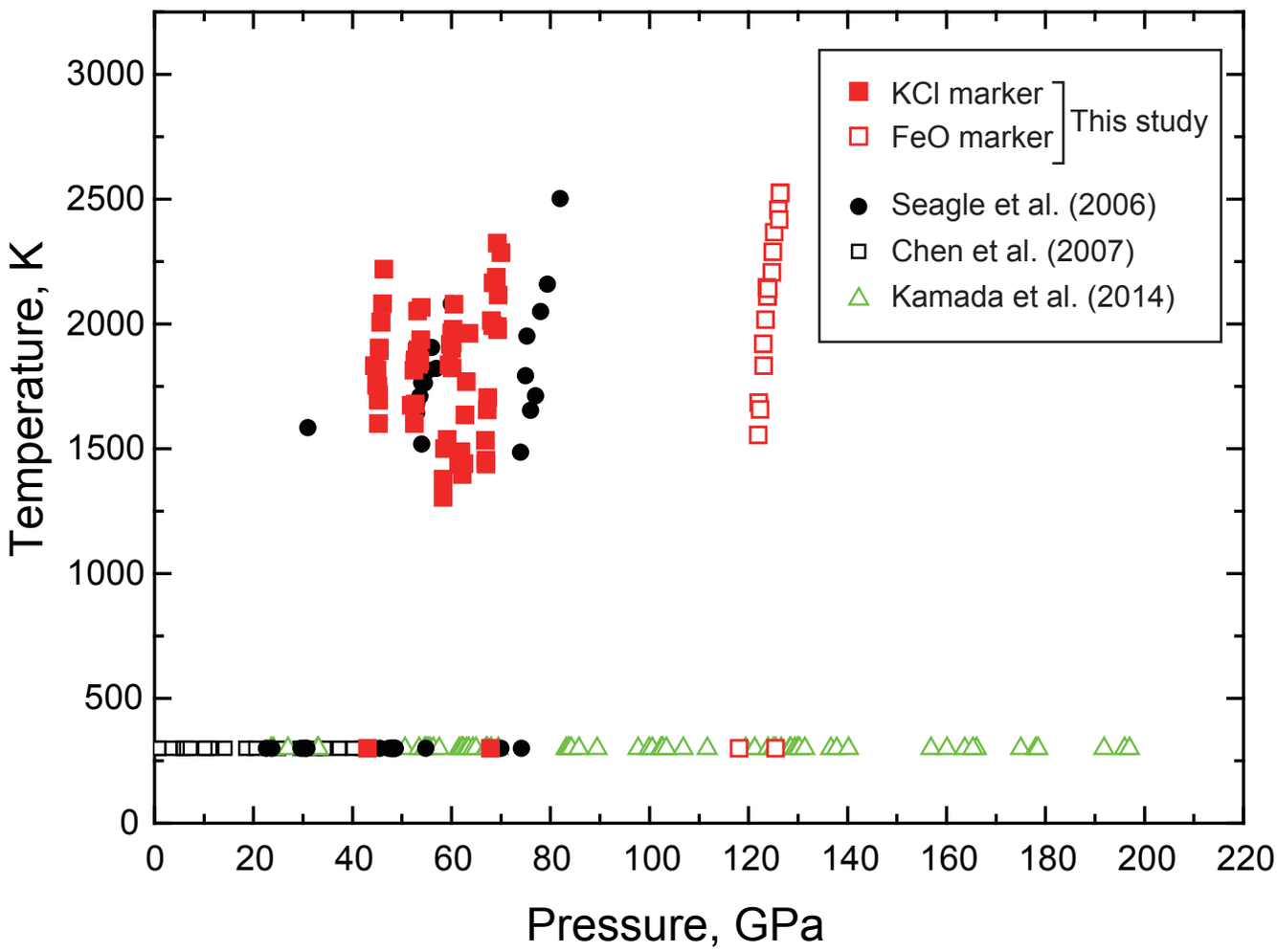
KCl marker
FeO marker
This study
Seagle et al. (2006)
Chen et al. (2007)
Kamada et al. (2014)
Temperature, K
Pressure, GPa
0
500
1000
1500
2000
2500
3000
0
20
40
60
80
100
120
140
160
180
200
220

Figure 1

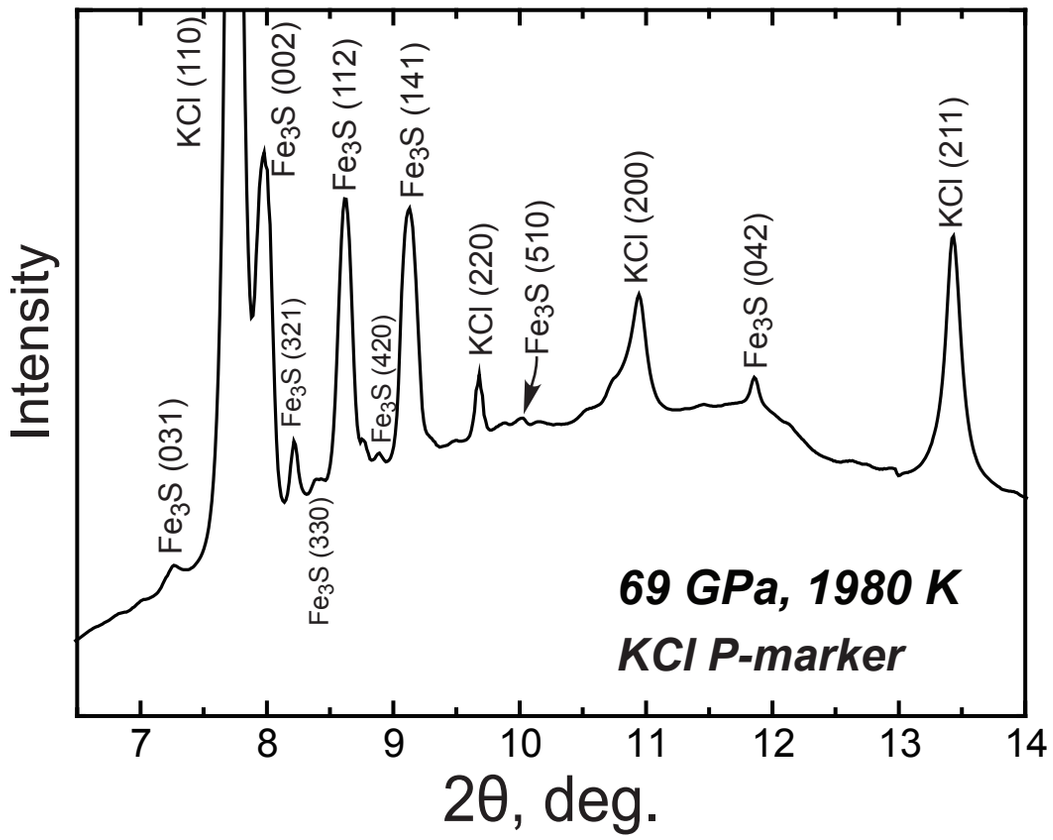
Intensity
KCl (110)
Fe3S (002)
Fe3S (112)
Fe3S (141)
Fe3S (031)
Fe3S (321)
Fe3S (330)
Fe3S (420)
KCl (220)
Fe3S (510)
KCl (200)
Fe3S (042)
KCl (211)
69 GPa, 1980 K
KCl P-marker
7
8
9
10
11
12
13
14
2θ, deg.

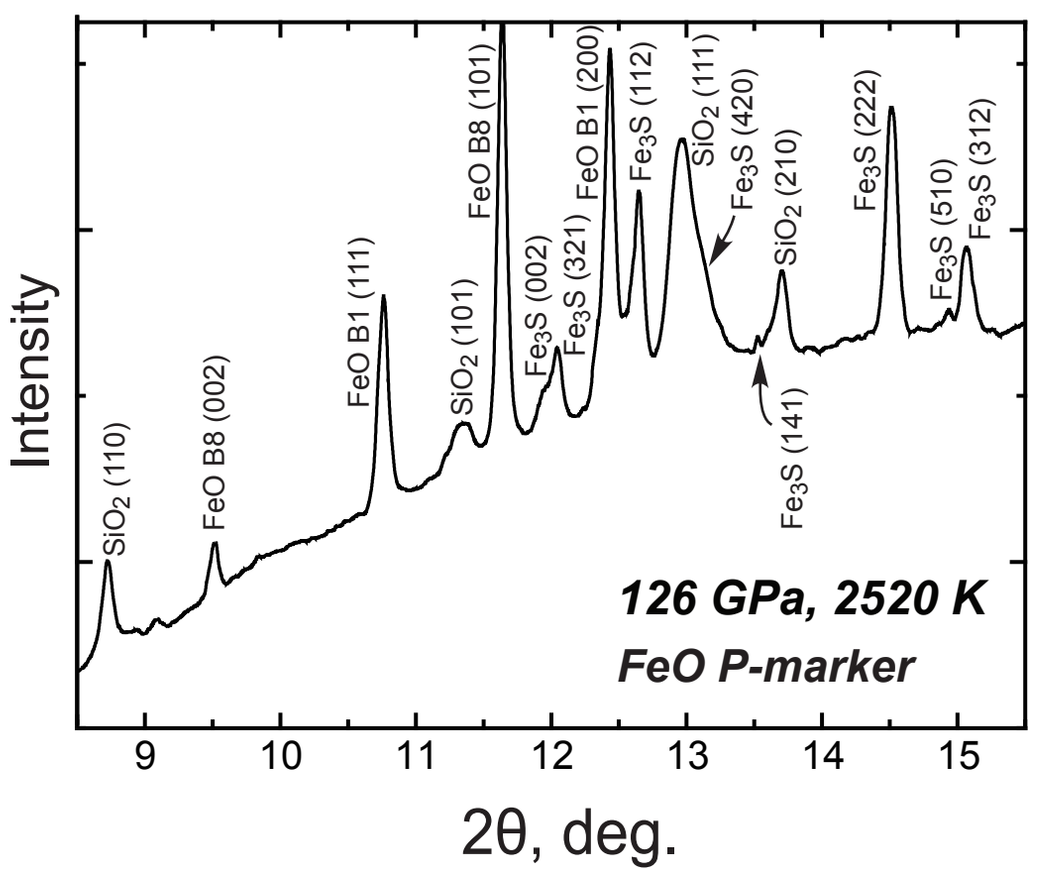
Intensity
SiO2 (110)
FeO B8 (002)
FeO B1 (111)
SiO2 (101)
FeO B8 (101)
Fe3S (002)
Fe3S (321)
FeO B1 (200)
Fe3S (112)
SiO2 (111)
Fe3S (420)
SiO2 (210)
Fe3S (141)
Fe3S (222)
Fe3S (510)
Fe3S (312)
126 GPa, 2520 K
FeO P-marker
9
10
11
12
13
14
15
2θ, deg.

Figure 2

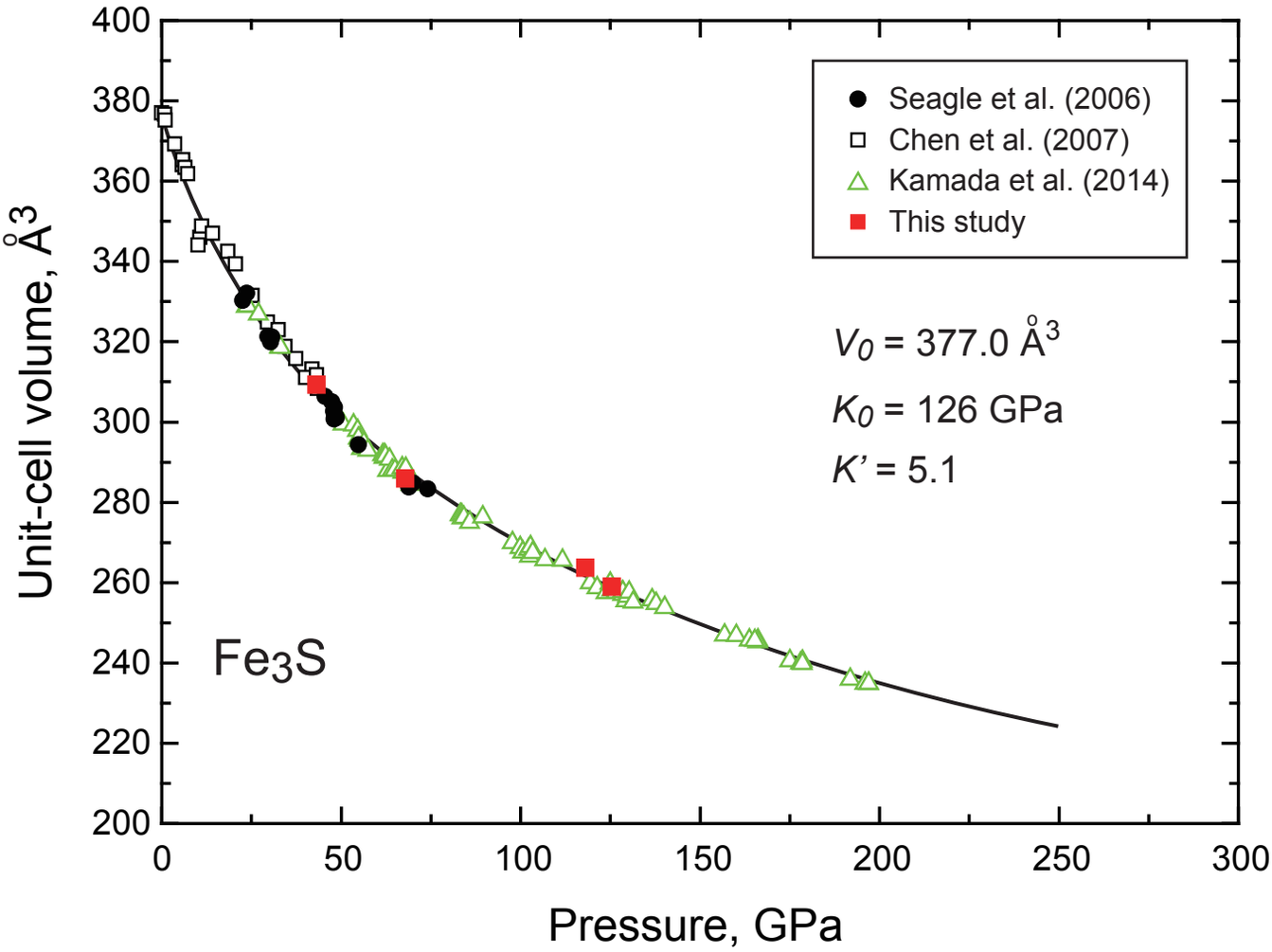
Unit-cell volume, Å3
Pressure, GPa
Seagle et al. (2006)
Chen et al. (2007)
Kamada et al. (2014)
This study
V0 = 377.0 Å3
K0 = 126 GPa
K' = 5.1
Fe3S
400
380
360
340
320
300
280
260
240
220
200
0
50
100
150
200
250
300

Figure 3

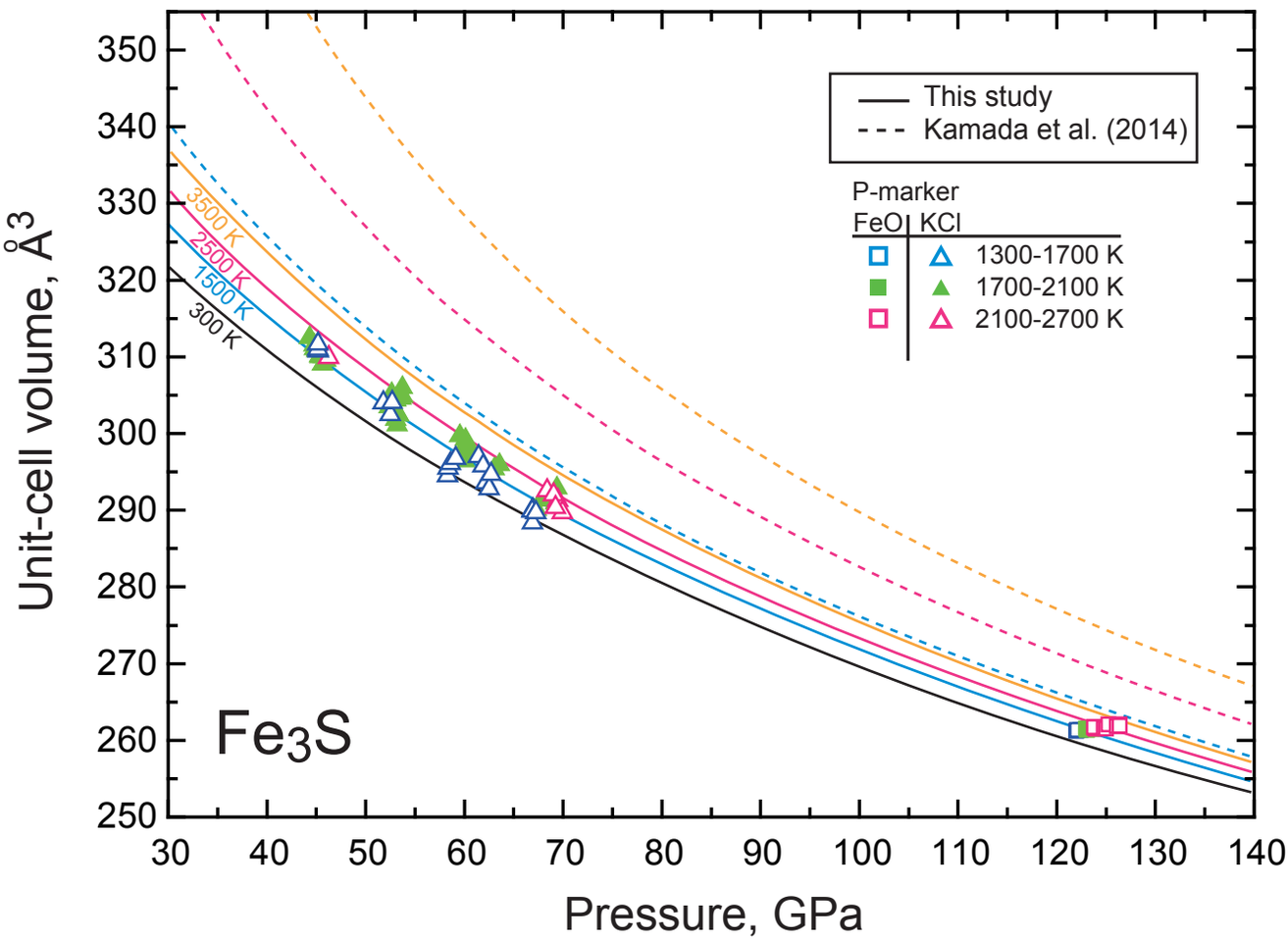
This study
Kamada et al. (2014)
P-marker
FeO KCl
1300-1700 K
1700-2100 K
2100-2700 K
3500 K
2500 K
1500 K
300 K
Fe3S
Unit-cell volume, Å3
Pressure, GPa
350
340
330
320
310
300
290
280
270
260
250
30
40
50
60
70
80
90
100
110
120
130
140

Figure 4

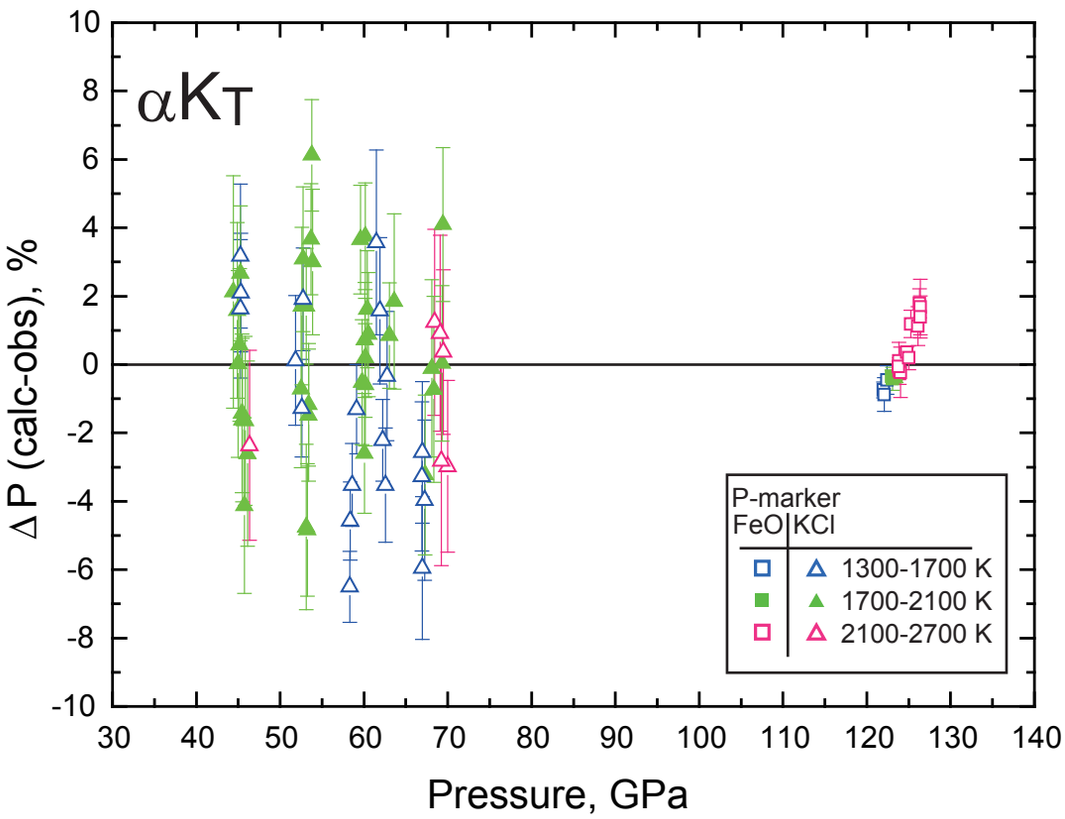
αKT
ΔP (calc-obs), %
Pressure, GPa
P-marker
FeO|KCl
1300-1700 K
1700-2100 K
2100-2700 K

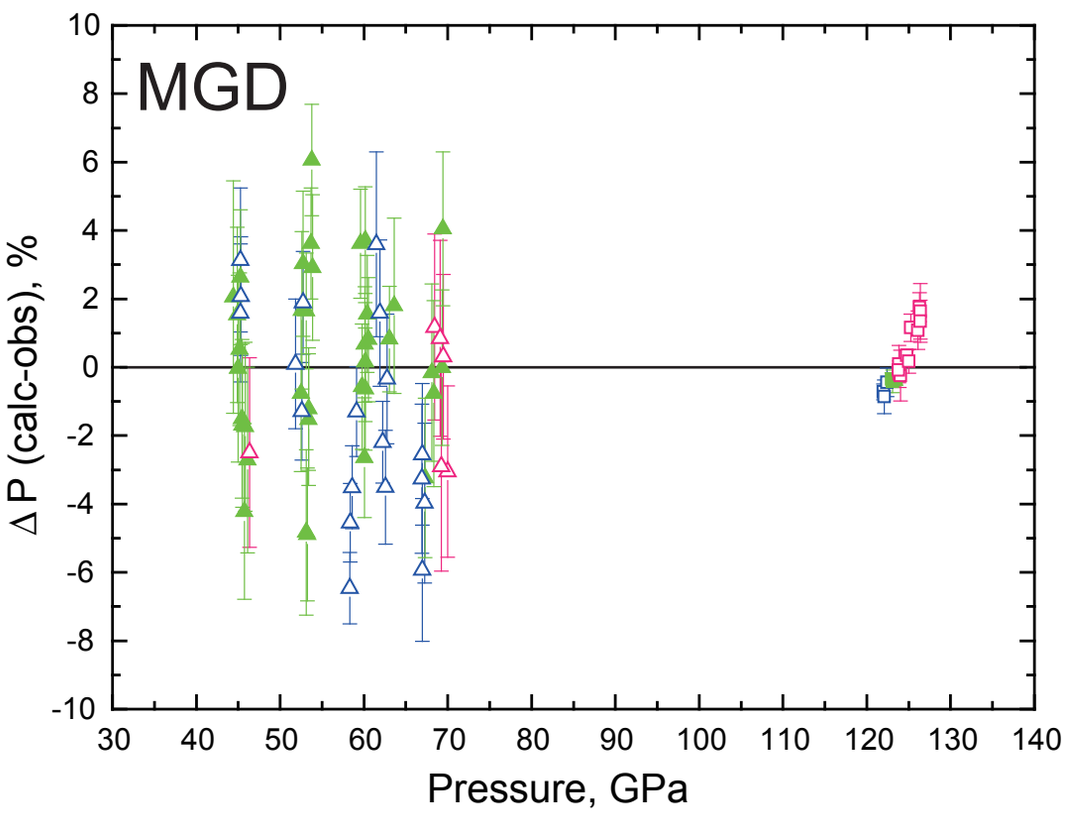
MGD
ΔP (calc-obs), %
Pressure, GPa

Figure 5

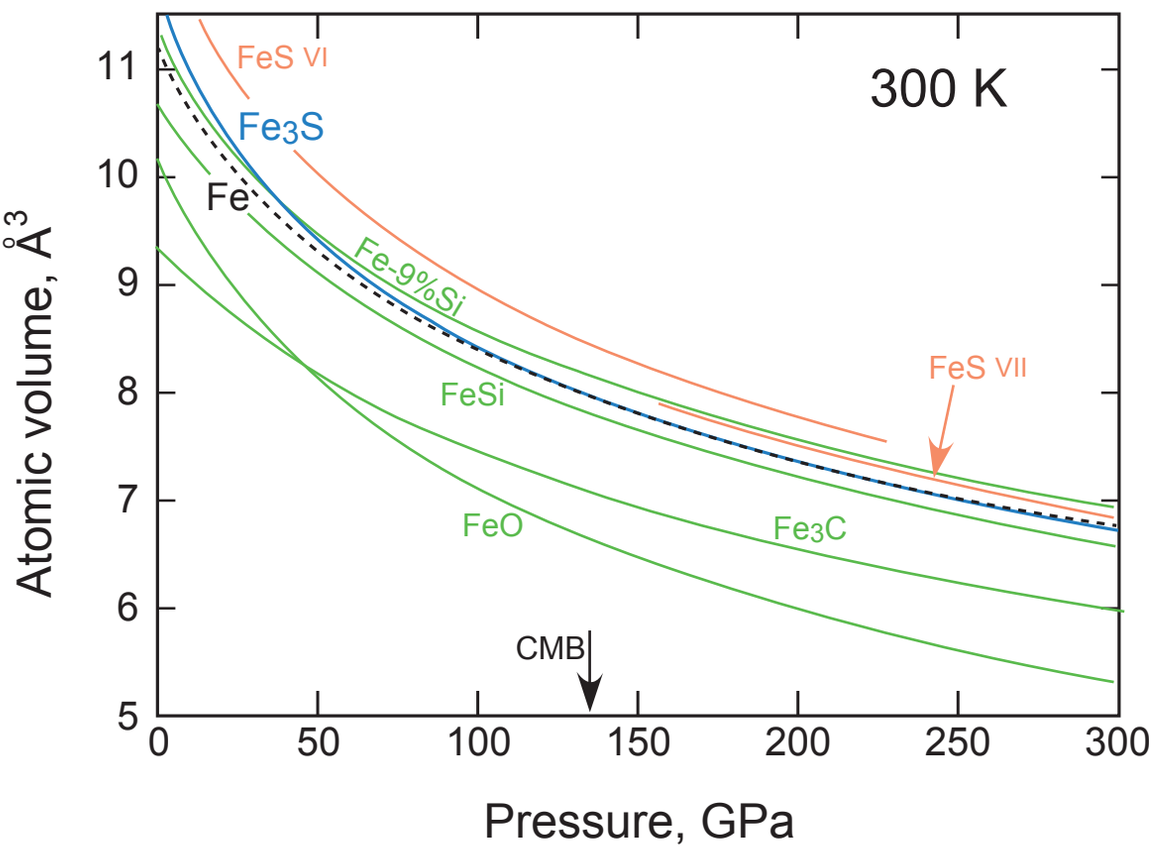
300 K
FeS VI
Fe3S
Fe
Fe-9%Si
FeSi
FeS VII
FeO
Fe3C
CMB
Atomic volume, Å3
Pressure, GPa
11
10
9
8
7
6
5
0
50
100
150
200
250
300

Figure 6

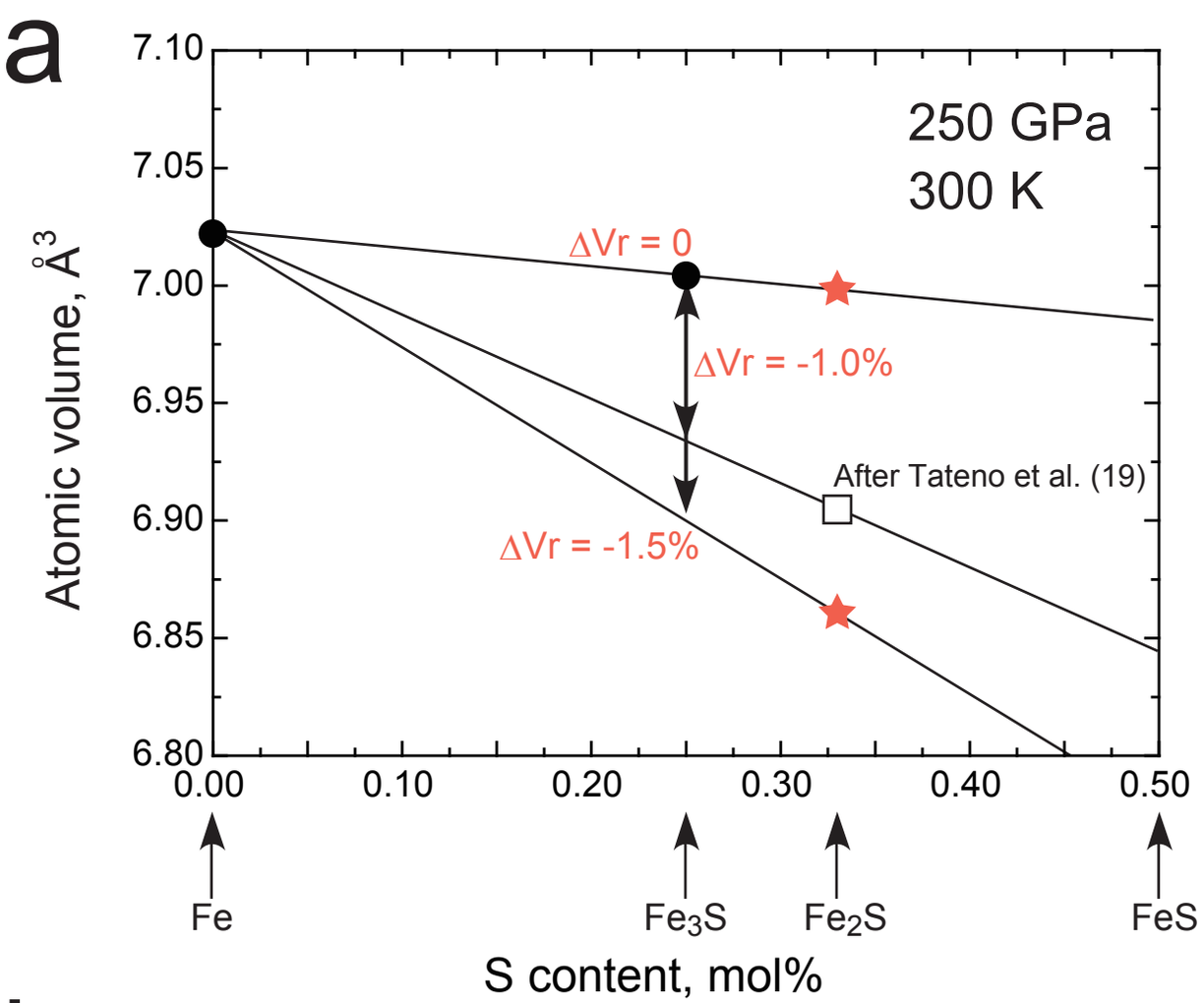
a
250 GPa
300 K
ΔVr = 0
ΔVr = -1.0%
ΔVr = -1.5%
After Tateno et al. (19)
Atomic volume, Å3
7.10
7.05
7.00
6.95
6.90
6.85
6.80
0.00
0.10
0.20
0.30
0.40
0.50
Fe
Fe3S
Fe2S
FeS
S content, mol%

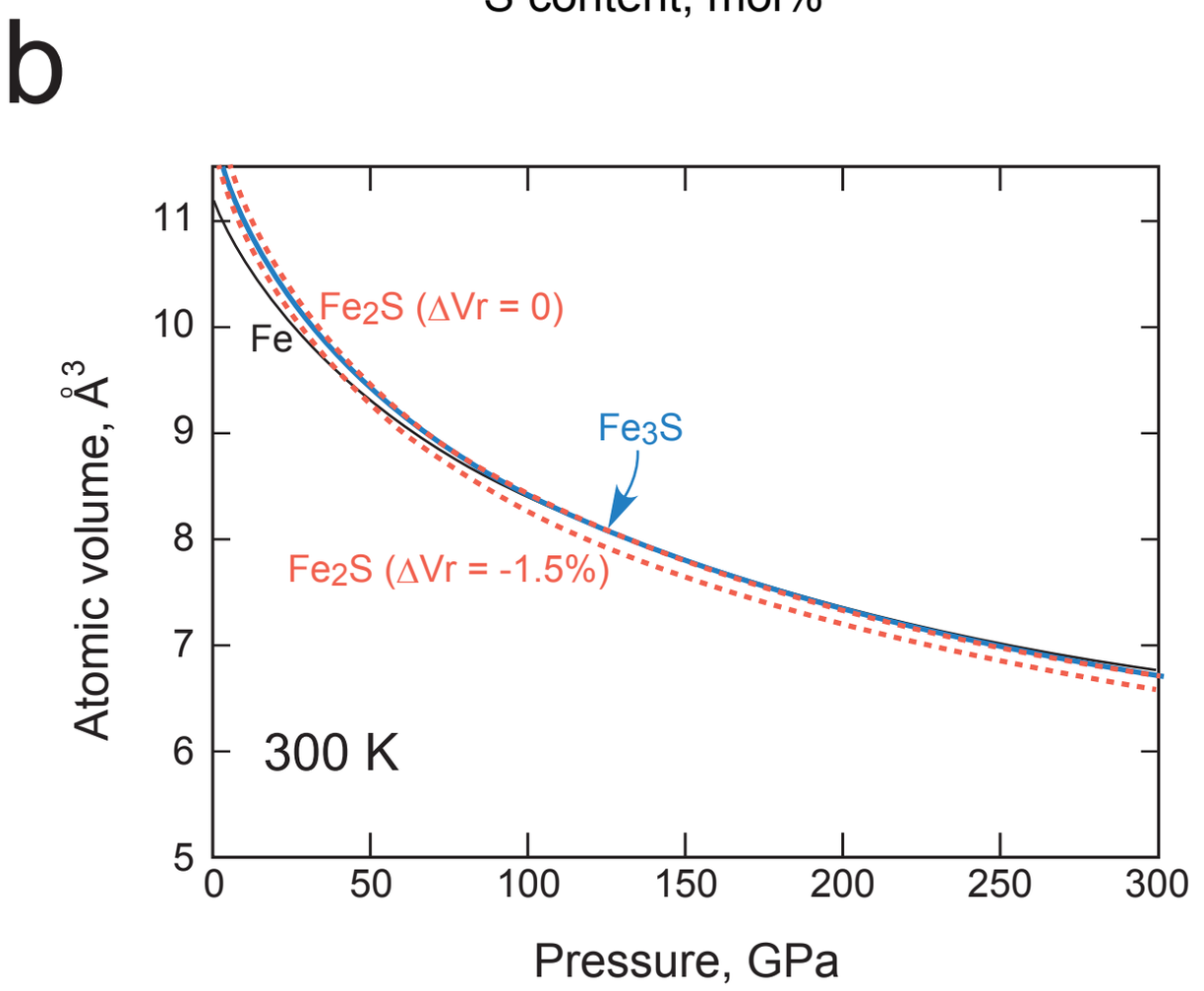
b
Fe2S (ΔVr = 0)
Fe
Fe3S
Fe2S (ΔVr = -1.5%)
300 K
Atomic volume, Å3
11
10
9
8
7
6
5
0
50
100
150
200
250
300
Pressure, GPa

Figure 7

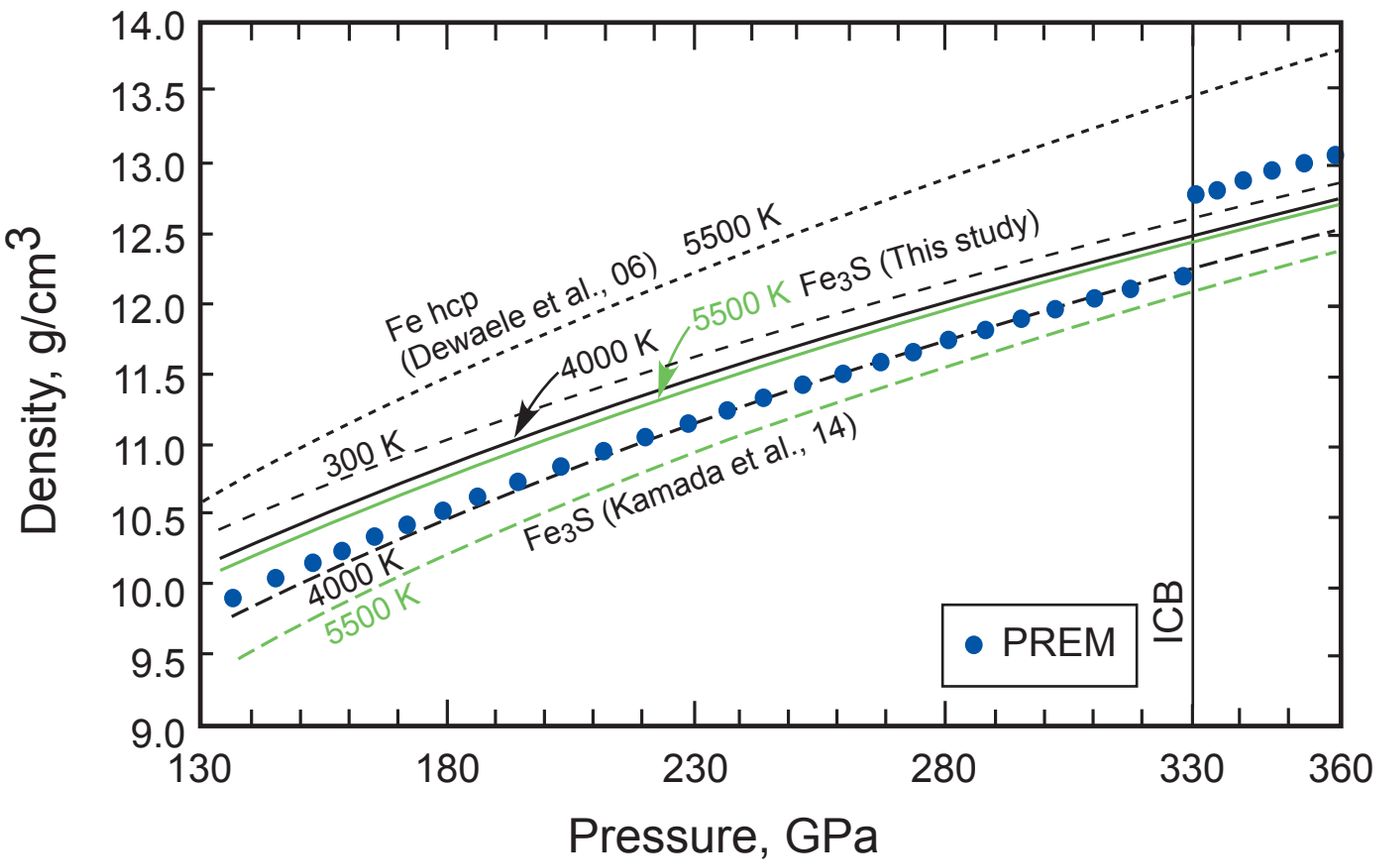
a
Density, g/cm3
Pressure, GPa
Fe hcp
(Dewaele et al., 06)
5500 K
4000 K
300 K
5500 K Fe3S (This study)
Fe3S (Kamada et al., 14)
4000 K
5500 K
PREM
ICB

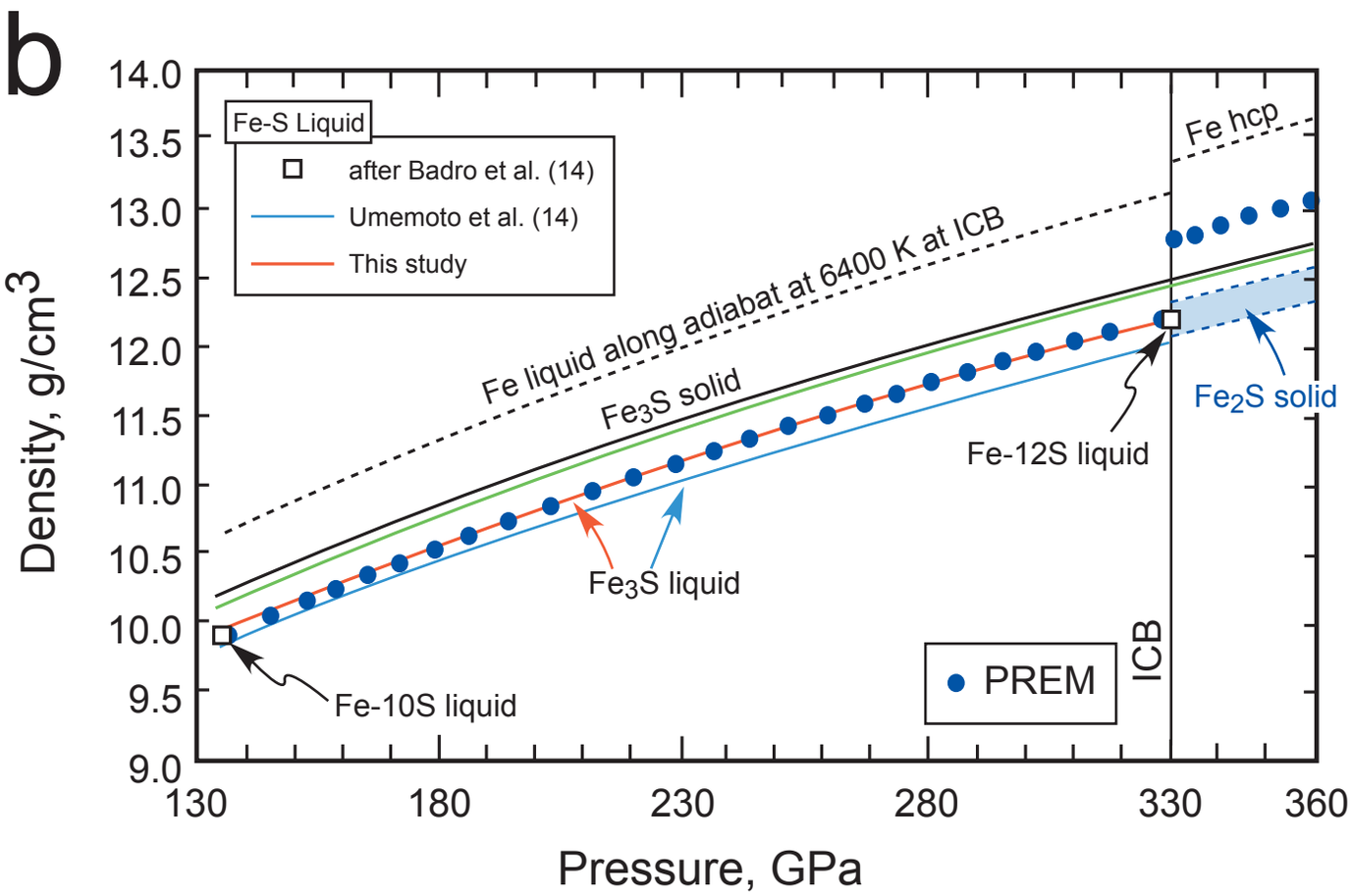
b
Density, g/cm3
Pressure, GPa
Fe-S Liquid
after Badro et al. (14)
Umemoto et al. (14)
This study
Fe hcp
Fe liquid along adiabat at 6400 K at ICB
Fe3S solid
Fe2S solid
Fe-12S liquid
Fe3S liquid
Fe-10S liquid
PREM
ICB

Figure 8

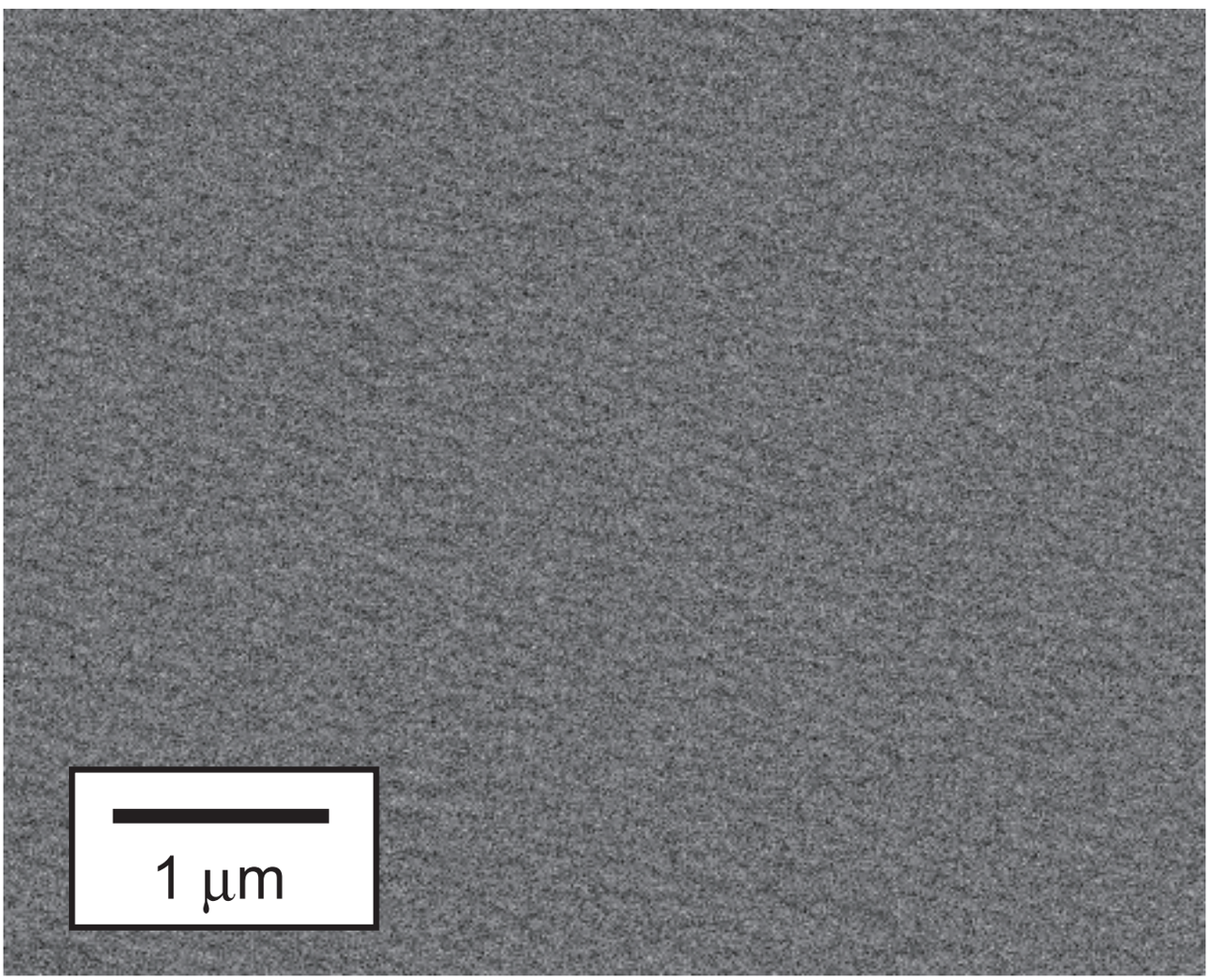

Fig. S1. Back scattered electron image of starting material with a composition of Fe_3S. The texture is highly homogeneous in composition.

126.4 GPa, 2530 K at BL10XU

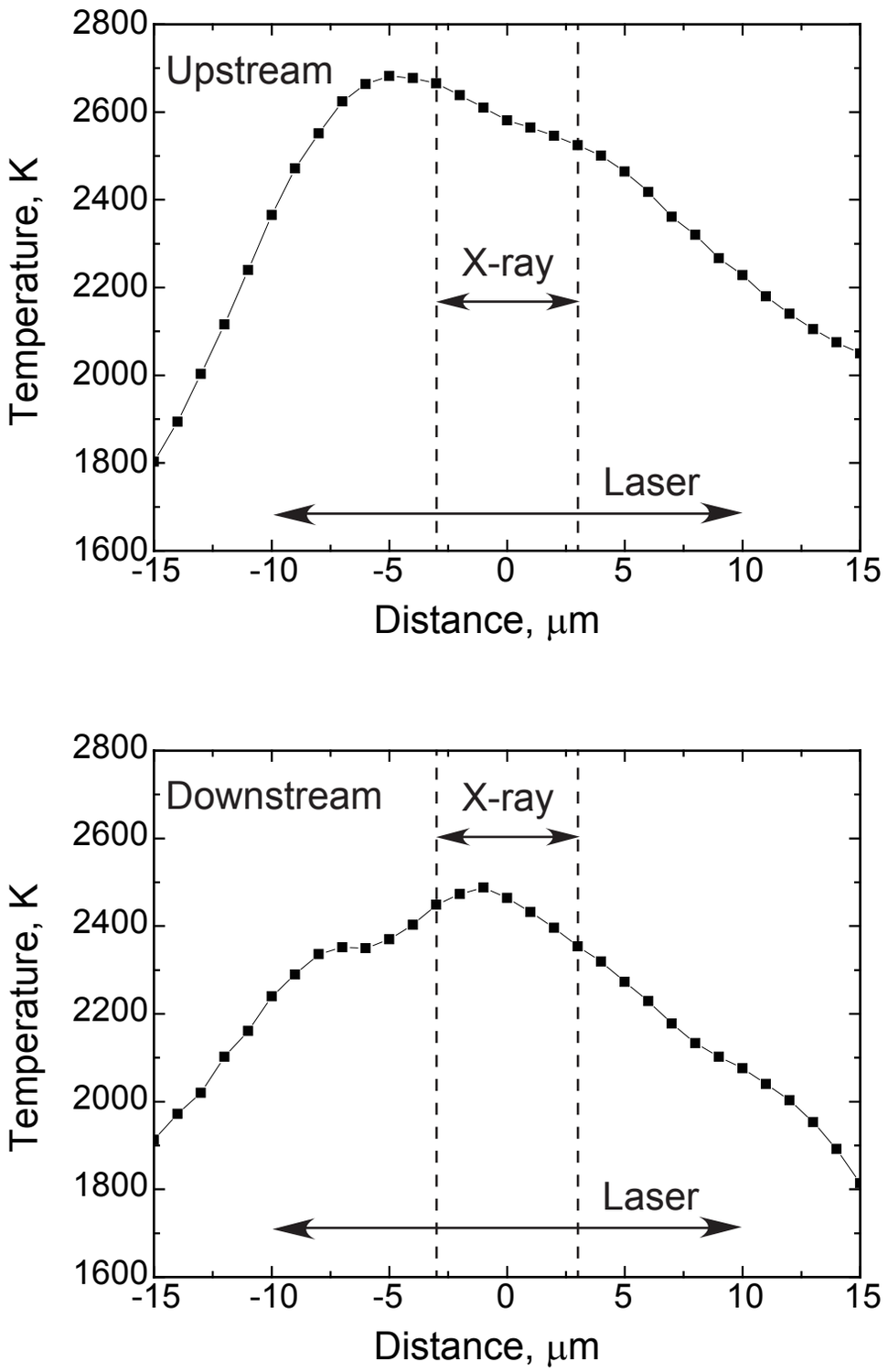

Fig. S2. Temperature distribution profile across the heated spot during laser heating in heating cycle 6. The laser heating was conducted on both sides. Upstream/downstream refers to the X-ray path. The X-rays probed much smaller areas than the heating laser spots to minimise the temperature gradient for XRD measurements.